

RESEARCH ARTICLE

A Model of Yeast Cell-Cycle Regulation Based on a Standard Component Modeling Strategy for Protein Regulatory Networks

Teeraphan Laomettachit^{1‡}, Katherine C. Chen², William T. Baumann³, John J. Tyson^{2*}

1 Genetics, Bioinformatics, and Computational Biology Program, Virginia Polytechnic Institute and State University, Blacksburg, Virginia, United States of America, **2** Department of Biological Sciences, Virginia Polytechnic Institute and State University, Blacksburg, Virginia, United States of America, **3** Department of Electrical and Computer Engineering, Virginia Polytechnic Institute and State University, Blacksburg, Virginia, United States of America

‡ Current address: Bioinformatics and Systems Biology Program, King Mongkut's University of Technology Thonburi, Bang Khun Thian, Bangkok 10150, Thailand

* tyson@vt.edu



CrossMark
click for updates

OPEN ACCESS

Citation: Laomettachit T, Chen KC, Baumann WT, Tyson JJ (2016) A Model of Yeast Cell-Cycle Regulation Based on a Standard Component Modeling Strategy for Protein Regulatory Networks. PLoS ONE 11(5): e0153738. doi:10.1371/journal.pone.0153738

Editor: Jordi Garcia-Ojalvo, Universitat Pompeu Fabra, SPAIN

Received: March 18, 2015

Accepted: April 4, 2016

Published: May 17, 2016

Copyright: © 2016 Laomettachit et al. This is an open access article distributed under the terms of the [Creative Commons Attribution License](https://creativecommons.org/licenses/by/4.0/), which permits unrestricted use, distribution, and reproduction in any medium, provided the original author and source are credited.

Data Availability Statement: C++ programs are included as Supporting Information.

Funding: This work was supported in part by a fellowship to TL from the Higher Educational Strategic Scholarships for Frontier Research Network of the Thai government, and by grants from the US National Institutes of Health to JJT and WBT (R01 GM078989) and to JJT and TM Murali (R01 GM095955).

Competing Interests: The authors have declared that no competing interests exist.

Abstract

To understand the molecular mechanisms that regulate cell cycle progression in eukaryotes, a variety of mathematical modeling approaches have been employed, ranging from Boolean networks and differential equations to stochastic simulations. Each approach has its own characteristic strengths and weaknesses. In this paper, we propose a “standard component” modeling strategy that combines advantageous features of Boolean networks, differential equations and stochastic simulations in a framework that acknowledges the typical sorts of reactions found in protein regulatory networks. Applying this strategy to a comprehensive mechanism of the budding yeast cell cycle, we illustrate the potential value of standard component modeling. The deterministic version of our model reproduces the phenotypic properties of wild-type cells and of 125 mutant strains. The stochastic version of our model reproduces the cell-to-cell variability of wild-type cells and the partial viability of the *CLB2-dbΔ clb5Δ* mutant strain. Our simulations show that mathematical modeling with “standard components” can capture in quantitative detail many essential properties of cell cycle control in budding yeast.

Introduction

The physiology of living cells is controlled by complex networks of interacting genes, proteins and metabolites [1]. These networks are often simplified by focusing on one level or another. A metabolic network treats genes and proteins as fixed parameters. A gene regulatory network focuses on how one gene controls another, skipping over the proteins that implement these control signals. A protein regulatory network, on the other hand, describes the production, degradation and post-translational modifications of proteins, without explicit reference to the nucleic acids that underpin protein synthesis. Such simplifications are entirely appropriate in

Abbreviations: CLE, chemical Langevin equation; MultiP, multisite phosphorylation; ODE, ordinary differential equation; PRN, protein regulatory network; SCM, standard component model; SSA, stochastic simulation algorithm.

certain circumstances, and the right way to model such networks also depends on the context. For instance, genetic control systems are often described by Boolean switching networks, where simple logical rules (Boolean functions) are used to describe the interactions among genes and to determine how the system updates its discrete state variables from one time-point to the next. Boolean models require no rate constants and are primarily used to capture the qualitative behavior of gene regulatory networks [2–4].

To describe the dynamical behavior of protein regulatory networks (PRNs), computational biologists have access to a range of mathematical modeling approaches, from discrete Boolean models to continuous models based on nonlinear ordinary differential equations (ODEs), to stochastic simulations with Gillespie-type models. ODE models are a common choice, because they track the evolution of a PRN continuously over time and their simulations can be compared in exquisite detail to experimental observations [5, 6]. The ODE approach, however, requires that the biochemical rate constants characterizing the reactions in the network be carefully estimated from experimental data. Parameter estimation for realistic models is a difficult task [7].

There have been some notable efforts to combine the advantageous features of ODE and Boolean models. Years ago Glass & Kauffman [8] used piecewise-linear differential equations to track continuous changes of protein concentrations (given by ODEs) in response to discrete changes in gene expression (given by a Boolean network). This approach was used elegantly by Uri Alon in his textbook on systems biology [9] and by a number of other research groups [10–12].

To incorporate molecular noise into network simulations, modelers have recourse to Gillespie's stochastic simulation algorithm (SSA) [13]—which simulates every reaction event and is statistically correct but comes at a high computational price—or less computationally expensive methods such as the chemical Langevin equation (CLE) [14] or stochastic Petri nets [15]. It is possible to include stochastic effects in Boolean models as well [16, 17].

Once a modeler adopts a particular quantitative approach, he or she faces the problem of choosing rate laws to represent the biochemical reactions in the network. Accurate stochastic modeling by SSA or CLE demands (in principle) that the network be described by elementary biochemical reactions with mass-action kinetics. ODE models are more flexible, and phenomenological rate laws (such as Michaelis-Menten kinetics, zero-order ultrasensitivity, and Hill functions) are often used. These phenomenological rate laws rely on some simplifications and assumptions that are, unfortunately, not always true in PRNs [18, 19].

To deal with the issues just described, we propose to model PRNs in terms of three classes of proteins, depending on the time scales of the reactions that govern their evolution. These three classes represent distinctly different “building blocks” of a network and are described by different types of mathematical equations. By connecting these building blocks in standard ways, we can construct a detailed model of a complex reaction network in a controlled fashion, much like a LEGO[®] toy. We refer to the output of this approach as a **standard component model** (SCM). Our approach combines many advantageous features of continuous, discrete and stochastic approaches, while organizing the model in a simple and logical format.

The goal of this paper is to demonstrate that the SCM approach can be applied effectively to model a complex protein regulatory network, namely the network regulating cyclin-dependent kinase activities during the cell division cycle of budding yeast. We build the model in two steps. First, we build a simple SCM of the *START* transition in the budding yeast cell cycle, to illustrate the general principles of deterministic and stochastic modeling by the standard-component method. Then we build a more complex SCM of the full cell division cycle of budding yeast, and test its accuracy by detailed comparisons to experimental data. Our presentation follows this outline:

1. Deterministic modeling by the standard-component method.
2. Molecular cell biology of the *START* transition in budding yeast.
3. A “multisite phosphorylation” (MultiP) model of the *START* transition.
4. A deterministic SCM of the *START* Transition
5. A stochastic version of the SCM.
6. Comparison of the SCM and MultiP models of the *START* transition.
7. An SCM of the full cell-cycle control system in budding yeast.
8. Deterministic simulations of the full SCM and comparison to the phenotypes of wild-type and mutant cells.
9. A stochastic version of the full SCM.
10. Comparison of stochastic simulations to the cell-to-cell variations exhibited by wild-type and mutant yeast cells.

Results

1. Deterministic SCM

Proteins regulate one another by controlling their abundances through rates of synthesis and degradation and their activities through post-translational modification (e.g., phosphorylation and dephosphorylation), and by associating into multisubunit complexes. These three classes of reactions often proceed on different time scales. Synthesis and degradation cause rather slow changes in the total amount of a protein (time scale > 10 min). Phosphorylation and dephosphorylation cause faster changes in protein activity (time scale = 1–10 min). Rapid association and dissociation of protein complexes bring the complexes and subunits into equilibrium on a short time scale (1 min or less). In cases where this separation of time scales is known or suspected to be the case, we can partition the components of a PRN into three classes:

Class-1 variables track the total amounts of proteins, which evolve rather slowly in time due to synthesis and degradation.

Class-2 variables track the activities of proteins, which change faster due to covalent modifications.

Class-3 variables track protein complexes, which turn over rapidly by association and dissociation of subunits.

In principle, variables of these three classes can represent different forms of the same protein. For example, we can use a class-1 variable to represent the total amount of a protein, while using a class-2 variable to represent the fraction of the total protein that is phosphorylated, and a class-3 variable to represent the fraction of the total protein that is bound to a stoichiometric inhibitor.

In our formalism, class-1 variables (X_i) are governed by pseudo-linear differential equations for protein synthesis and degradation

$$\frac{dX_i}{dt} = A_i - B_i \cdot X_i \quad (1)$$

The ODE is linear in X_i , the number of molecules of species X_i , but the rates of synthesis and degradation are functions of variables Y_j that may belong to any of the three classes. It is

often possible to use linear functions for A_i and B_i ,

$$A_i = \alpha_{i0} + \sum_{j \in \mathbf{J}} \alpha_{ij} \cdot Y_j \tag{2}$$

$$B_i = \beta_{i0} + \sum_{j \in \mathbf{J}} \beta_{ij} \cdot Y_j \tag{3}$$

where α_{i0} and β_{i0} are basal rates of synthesis and degradation, and $\alpha_{ij} \cdot Y_j$ and $\beta_{ij} \cdot Y_j$ are rates regulated by transcription factors and proteolytic enzymes, respectively. (In this case, the biochemical rate parameters α_{i0} , β_{i0} , α_{ij} , and β_{ij} are all positive constants.) In other cases—especially for transcription factors that inhibit gene expression—nonlinear functions for A_i and B_i may be required.

Class-2 variables are governed by nonlinear ODEs of the form

$$\frac{dY_j}{dt} = \gamma_j(Y_{j,T} \cdot H(\sigma_j \cdot W_j) - Y_j), \tag{4}$$

where Y_j represents the activity of protein Y_j (e.g., the phosphorylated or the active form of Y_j), $Y_{j,T}$ is the total number of molecules of protein Y_j , γ_j determines the time scale of the reaction, and $H(x) = 1/(1 + e^{-x})$ is the sigmoidal function illustrated in [S1 Fig](#). (H is a hyperbolic tangent function shifted along the y-axis. In population biology it is known as the “logistic” function. We refer to H as the “soft-Heaviside” function, because we use it to replace the step-like Heaviside function used in the piecewise-linear models of Glass, Kauffman and others.) In the soft-Heaviside function, W_j describes the net influence of all components in the network on the component Y_j :

$$W_j = \pm\omega_{j0} + \sum_{k \in \mathbf{K}} \omega_{jk} \cdot Y_k - \sum_{l \in \mathbf{L}} \omega_{jl} \cdot Y_l. \tag{5}$$

In [Eq 5](#), ω_{jk} and ω_{jl} are weights (always positive values) that describe the influences of variables Y_k and Y_l on the variable Y_j . \mathbf{K} represents all variables that have positive influences on the variable Y_j , and \mathbf{L} represents all variables that have negative influences on the variable Y_j . Y_k and Y_l can be variables of any of the three classes of species. The background influence, ω_{j0} , which can be preceded by either the positive or negative sign, determines the value of the soft-Heaviside function when protein Y_j is receiving no inputs from the other proteins in the network. The parameter σ_j controls the steepness of the soft-Heaviside function; see [S1 Fig](#). In principle, the value of σ_j could be absorbed into the values of the ω 's, but we prefer to treat σ_j as a separate parameter and to think of the ω 's as relative interaction strengths. That way, we can vary the steepness of the soft-Heaviside function independently of the relative interaction strengths and *vice versa*.

[Eq 4](#) shows that $H(\sigma_j \cdot W_j)$ determines the steady state of the variable Y_j as a fraction of the total amount $Y_{j,T}$. If the total amount of the protein remains constant over time, $Y_{j,T}$ is a constant parameter in the model. If the total amount of the protein changes in time, we can use a class-1 variable to keep track of $Y_{j,T}$ while using a class-2 variable to keep track of the fraction of the protein that is in the active form.

Class-2 variables evolve to a steady state on a time scale that is proportional to γ_j^{-1} . Therefore, if γ_j is large, we can invoke the pseudo-steady state approximation for the class-2 variable:

$$Y_j = Y_{j,T} \cdot H(\sigma_j \cdot W_j). \tag{6}$$

Moreover, if both γ_j and σ_j are large, then the class-2 variable, $Y_j/Y_{j,T}$, behaves like a Boolean variable, switching rapidly between 0 and 1 in response to other components in the network (S1 Fig).

Eq 4 has been used to describe interactions in PRNs many times before [12, 20–23]. We use the soft-Heaviside function because biochemical reactions (such as phosphorylation and dephosphorylation) are nonlinear in nature and often show ultrasensitive, sigmoidal responses [24–26]. Different mechanisms have been proposed to give rise to ultrasensitivity, and different types of rate equations have been used to capture this response. For transcription factors binding to gene promoter regions, Hill functions are often used to express the highly nonlinear (ultrasensitive) response of gene transcription rate to transcription factor concentration. For post-translational modifications of proteins, a commonly used mechanism is zero-order ultrasensitivity, originally proposed by Goldbeter & Koshland (GK) [25]. The GK equation describes the steady-state activity of a protein modified by two Michaelis-Menten enzymes with opposing effects (activation and inactivation). More recently, multisite phosphorylation has received considerable attention as an alternative mechanism of ultrasensitivity in PRNs [26–28]. All these mechanisms ultimately lead to sigmoidal-like responses, similar to the soft-Heaviside function (S1 Fig). Therefore, we eschew specific assumptions about the molecular mechanisms of ultrasensitivity and simply use the soft-Heaviside function as a phenomenological law that captures the ultrasensitive responses that are characteristic of PRNs.

Class-3 variables describe the rapid association and dissociation of proteins in multi-subunit complexes. For example, if proteins Y and I bind together strongly in an inactive complex, then the number of Y molecules that are free (not bound to I) is given by

$$Y = \max(0, Y_T - I_T). \tag{7}$$

This equation is a good approximation if both association and dissociation rates are fast, and the equilibrium binding constant is large. The max function returns zero if the total amount of the protein, Y_T , is less than the total amount of its inhibitor, I_T , meaning that all of protein Y is sequestered in the complex. On the other hand, if $Y_T > I_T$, then the free form of the protein, Y, is simply the excess of Y_T over I_T .

If an inhibitor associates with two different proteins with comparable association and dissociation rates, the amounts of the free proteins can be approximated by

$$\begin{aligned} Y_1 &= \max\left(0, \frac{Y_{1,T}}{Y_{1,T} + Y_{2,T}} \cdot (Y_{1,T} + Y_{2,T} - I_T)\right) \\ Y_2 &= \max\left(0, \frac{Y_{2,T}}{Y_{1,T} + Y_{2,T}} \cdot (Y_{1,T} + Y_{2,T} - I_T)\right) \\ I &= \max(0, I_T - Y_{1,T} - Y_{2,T}) \end{aligned} \tag{8}$$

where I_T , $Y_{1,T}$ and $Y_{2,T}$ are the total amounts of the proteins, and I , Y_1 and Y_2 are the amounts of the free forms of the proteins. In Eq 8, we assume that the inhibitor is distributed equally between Y_1 and Y_2 , according to the availability of the two proteins. If I binds much more strongly to Y_1 than to Y_2 , then Eq 8 should be replaced by

$$\begin{aligned} Y_1 &= \max(0, Y_{1,T} - I_T) \\ Y_2 &= \min\{\max(0, Y_{1,T} + Y_{2,T} - I_T), Y_{2,T}\} \\ I &= \max(0, I_T - Y_{1,T} - Y_{2,T}) \end{aligned} \tag{8'}$$

In the following sections, we show how to use these three classes of variables as building blocks to construct an SCM of the molecular network controlling the cell division cycle in budding yeast. Because the full model is very complex, we approach it in a series of simpler steps.

2. The Start transition in budding yeast

START is an event in G_1 phase of the budding yeast cell cycle when a cell commits to a new round of DNA synthesis and mitosis. A crucial step of the START transition is the translocation of Whi5, a stoichiometric inhibitor of SBF and MBF transcription factors, from nucleus to cytoplasm [29, 30]. SBF and MBF control the expression of *CLN2* and *CLB5* genes, which encode “cyclin” proteins Cln2 and Clb5, respectively. Cln2 and Clb5 bind to kinase subunits (Cdc28) to form heterodimers with “cyclin-dependent kinase” (CDK) activity. CDK activity generated at START triggers initiation of DNA synthesis and bud emergence. Because kinase subunits are in excess over cyclin partners [31], CDK activity is determined solely by the abundance of cyclin proteins. For simplicity in illustrating the SCM approach for the START transition, we combine Cln2- and Clb5-dependent kinase activities into a single variable, called ClbS. We also treat SBF and MBF as a single variable, called SBF.

During normal cell cycle progression in budding yeast, the cell needs to grow sufficiently large to execute START [32, 33]. The major players involved in “size control” of START are Cln3 and Whi5. Whi5 prevents the START transition by binding to and inhibiting SBF, and Cln3 promotes START by phosphorylating and inactivating Whi5 [29,30]. The accumulation of Cln3 in G_1 phase seems to depend on cell growth [34], and recent evidence suggests that Whi5 concentration is diluted out by cell growth [35]. As the cell grows, Cln3-dependent kinase phosphorylates Whi5, resulting in translocation of Whi5 from nucleus to cytoplasm and the release of its inhibition on SBF. Free SBF promotes the synthesis of ClbS, which stimulates its own expression by further phosphorylating Whi5. This positive feedback loop is thought to enforce the irreversible commitment of cells to the START transition [36]. A schematic diagram illustrating the molecular basis of the START transition is shown in Fig 1A.

Before constructing an SCM of the START transition, we first describe a multisite phosphorylation (MultiP) model that will serve as a “reference point” for judging the adequacy of the SCM.

3. A multisite phosphorylation model of the Start transition

Our MultiP model is a simplified version of a model developed by Barik *et al.* [27] (see Fig 1B), who used mass-action kinetics to describe all the reactions involved in the START transition and carried out detailed stochastic simulations based on Gillespie’s algorithm [13]. Our version of the model (see the equations in S1 Text) is governed by 20 molecular species, including both proteins and mRNAs (m_{n3} , m_{bS} , m_{i5} , and m_{hi5} are mRNAs for Cln3, ClbS, Whi5, and Hi5, respectively). The 20 molecular species participate in 50 reactions, representing synthesis, degradation, phosphorylation, dephosphorylation, association, and dissociation of the species. Mass-action rate laws are used for all reactions. Each differential equation specifies how the number of molecules of each species changes with time.

Cell size (V) is assumed to increase exponentially. The rate of synthesis of each protein is assumed to be proportional to volume $V \times$ number of mRNA molecules m encoding the protein, because we assume that the number of ribosomes per cell increases proportionally to cell size V . In this way, we ensure that the concentration (N/V) of every constitutively expressed protein remains constant as the cell grows. The only exception is Cln3, whose synthesis rate—we assume—is proportional to the square of cell size (V^2), as in Barik’s model [27]. This assumption, whose consequence is that the concentration of Cln3 increases exponentially as

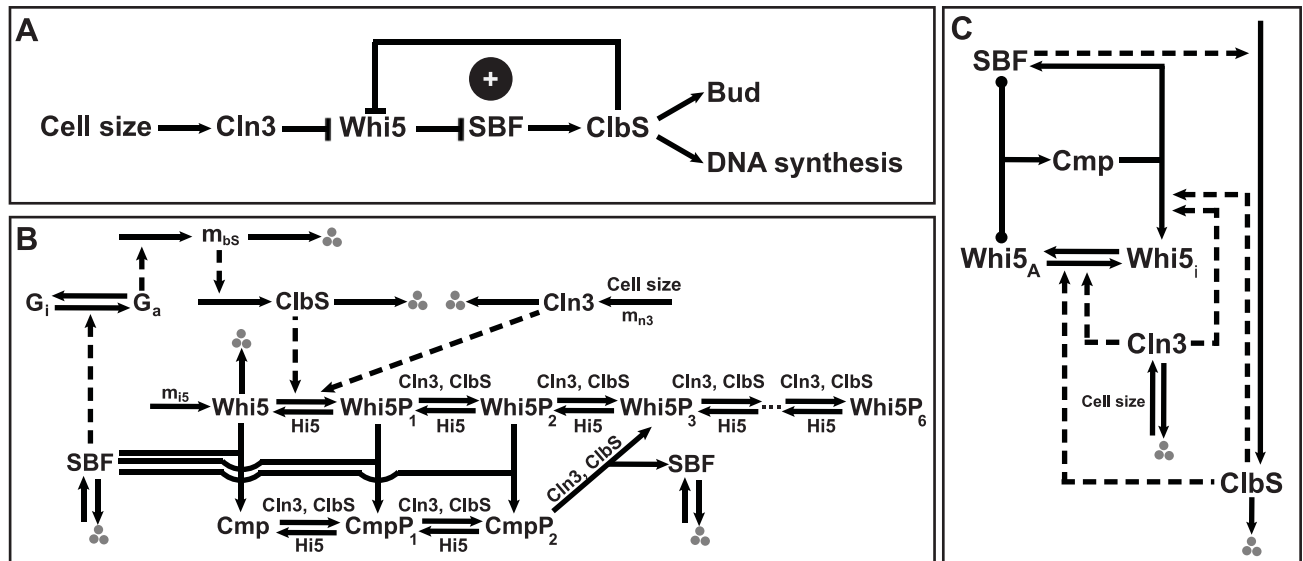


Fig 1. The Start transition. (A) Schematic diagram of the START transition in budding yeast. In early G₁, SBF is inactivated by its stoichiometric inhibitor, Whi5. As cell size increases, Cln3 accumulates and begins to phosphorylate Whi5. Phosphorylated Whi5 loses its ability to bind to SBF. As a result, SBF is free and promotes the production of ClbS (Cln2 and Clb5). ClbS exerts positive feedback on its own accumulation by further phosphorylating Whi5. The activation of SBF correlates with the onset of the START transition. Subsequent accumulation of ClbS promotes both bud emergence and the G₁/S transition. (B) Wiring diagram of the MultiP model. The first three forms of Whi5 (Whi5, Whi5P₁, and Whi5P₂) bind to SBF and inhibit its ability to activate the synthesis of ClbS. The higher phosphorylated forms are inactive and do not bind to SBF. The model also includes mRNA species for each protein component. (C) Wiring diagram of the standard component model. The 10 distinct forms of Whi5 in the MultiP model are replaced by two forms of Whi5 (active and inactive). For panels B and C, solid lines indicate chemical reactions (synthesis and degradation, phosphorylation and dephosphorylation, association and dissociation) and dashed lines indicate activatory or inhibitory influences of components on chemical reactions.

doi:10.1371/journal.pone.0153738.g001

the cell grows, introduces a “size dependence” on the START transition, which is needed to account for many properties of cell cycle progression in budding yeast. Although this assumption is sufficient to account for the observed size-dependence of yeast cell division, it is certainly not necessary. Other explanations are possible. Indeed, Schmoller *et al.* [35] have recently shown that Cln3 synthesis rate increases in direct proportion to V , so that its total concentration is nearly constant during G₁ phase; and size dependence of the yeast cell cycle depends on diluting out Whi5, an inhibitor of START, as the cell grows. This alternative will be explored in future versions of the model.

In Barik’s model [27], multisite phosphorylation of Whi5 is the source of nonlinearity necessary for the ultrasensitive START transition. Whi5 is phosphorylated *in vivo* on ~10 CDK phosphorylation sites [37]. In Barik’s model Whi5 has seven phosphorylated states: Whi5, Whi5P₁, Whi5P₂, . . . , Whi5P₆. In the model, the sites are phosphorylated sequentially and distributively [26]. The first three forms bind rapidly and strongly to SBF; the higher phosphorylated states (Whi5P₃, . . . , Whi5P₆) are inactive and unable to bind to SBF. Free SBF binds to and activates the ClbS gene ($G_i + SBF \leftrightarrow G_a$). Cln3 and ClbS phosphorylate Whi5 (both free and in complex with SBF), while Whi5P_i species are dephosphorylated by an unspecified phosphatase, called Hi5 (“H” for phosphatase, “i5” for Whi5).

In Barik’s model [27], Whi5:SBF complexes are called Cmp, CmpP₁, and CmpP₂. Whi5P₂ in the complex (CmpP₂) is assumed not to get further phosphorylated. For Whi5P₂ in the complex to be phosphorylated and thereby inactivated, Barik’s model supposes that Whi5P₂ must first dissociate from CmpP₂. We think this requirement is unnecessarily restrictive, so we allow the doubly-phosphorylated Whi5 in the complex (CmpP₂) to be further phosphorylated, and

the triply-phosphorylated *Whi5* is assumed to immediately release SBF. We also assume, in the MultiP model, that the dissociation rate of SBF:*Whi5P_i* complexes is negligible.

4. An SCM for the Start transition

[Fig 1C](#) is the SCM representation of the *START* transition. We assign the components in this diagram to the three classes of variables proposed above.

Cln3 and *Clb5* are described by class-1 variables:

$$\frac{dCln3}{dt} = k_{s,n3} \cdot V^2 \cdot \underbrace{\frac{k_{s,mn3}}{k_{d,mn3}}}_{m_{n3}} - k_{d,n3} \cdot Cln3 \tag{9}$$

$$\frac{dClbS}{dt} = k_{s,bs} \cdot V \cdot \underbrace{\frac{k_{s,mbS}}{k_{d,mbS}} \cdot \left(\frac{SBF}{SBF + \frac{k_{d,g} \cdot V}{k_{a,g}}} \right)}_{G_a}_{m_{bS}} - k_{d,bs} \cdot ClbS. \tag{10}$$

In these equations, V = cell size, which we assume increases exponentially in time, $V(t) = V_0 e^{\mu t}$, where μ is the specific growth rate of the cell. For each protein, its rate of synthesis is the product of (rate of translation, $k_{s,\dots}$) \times (number of mRNAs, m_{\dots}) \times (cell size, V). We explicitly account for the number of mRNAs in our synthesis rates (the factors labeled m_{n3} and m_{bS}), as the mRNA number will be important later for representing noise terms. For simplicity, we assume (in the deterministic SCM) that mRNAs are always at their steady state levels. As in the MultiP model, we assume that the synthesis rate of *Cln3* is proportional to the square of cell size (V^2) so that the concentration of *Cln3* (number/volume) will increase exponentially as the cell grows. The activity of the gene encoding *Clb5*, G_a , depends on active SBF binding to the promoter region of the gene.

Since multisite phosphorylation of *Whi5* gives rise to its ultrasensitive response to total CDK activity, we use a class-2 variable for the active form of *Whi5* and a class-1 variable for the total amount of *Whi5*:

$$\frac{dWhi5_A}{dt} = \gamma \cdot (Whi5_T \cdot H(\sigma \cdot W_{i5}) - Whi5_A) \tag{11}$$

$$W_{i5} = \frac{\omega_{dp,i5}}{V} \cdot Hi5 - \frac{\omega_{p,i5}}{V} \cdot Cln3 - \frac{\omega'_{p,i5}}{V} \cdot ClbS \tag{12}$$

$$\frac{dWhi5_T}{dt} = k_{s,i5} \cdot V \cdot \underbrace{\left(\frac{k_{s,mhi5}}{k_{d,mhi5}} \right)}_{m_{i5}} - k_{d,i5} \cdot Whi5_T \tag{13}$$

$$\frac{dHi5}{dt} = k_{s,hi5} \cdot V \cdot \underbrace{\left(\frac{k_{s,mhi5}}{k_{d,mhi5}} \right)}_{m_{hi5}} - k_{d,hi5} \cdot Hi5 \tag{14}$$

where $H(x)$ is the soft-Heaviside function defined earlier (see [S1 Fig](#)). We assume that the phosphorylation and dephosphorylation of *Whi5* are independent of its binding state to SBF. In

this way, we are able to use two differential equations (Eqs 11 and 13) to represent 10 distinct states of Whi5 and Whi5:SBF complexes. Here, $Whi5_A$ (Eq 11) represents the total amount of active Whi5 both free and bound to SBF (it includes $Whi5$, $Whi5P_1$, $Whi5P_2$, Cmp , $CmpP_1$, and $CmpP_2$ in the MultiP model); whereas ($Whi5_T - Whi5_A$) represents the other four inactive forms of Whi5 ($Whi5P_3$ to $Whi5P_6$). Hi5 (the phosphatase that re-activates Whi5) is described by a class-1 variable in Eq 14.

In Eq 12, the interaction coefficients $\omega_{p,i5}$, $\omega'_{p,i5}$ and $\omega_{dp,i5}$ are all positive numbers. The signs—positive or negative—in front of each term determine whether the interaction is activating or inhibiting (dephosphorylation or phosphorylation, in this case).

Assuming that binding between active forms of Whi5 and SBF is rapid and strong, we describe free SBF as a class-3 variable

$$SBF = \max(0, SBF_T - Whi5_A) . \tag{15}$$

This equation indicates that free SBF is equal to the excess of the total SBF over the total active Whi5, where SBF_T (Eq 16) is represented by a class-1 variable.

$$\frac{dSBF_T}{dt} = k_{s,bf} \cdot V - k_{d,bf} \cdot SBF_T \tag{16}$$

Because the original model of Barik *et al.* [27] did not have an mRNA species for SBF, we have not included mRNA for SBF in the SCM.

Using the SCM approach, we reduce the complexity of the START model to seven differential equations plus one algebraic equation (from 20 equations in S1 Text for the MultiP model). The parameter values used in the SCM (Table 1) are inherited, for the most part, from the parameter values in Barik *et al.* [27]. The parameter values assigned by Barik *et al.* were estimated from experimental data wherever possible. For example, protein degradation rates were calculated from protein half-life measurements in the literature, and synthesis rate constants were assigned to agree with the average number of protein molecules observed for an asynchronous population of yeast cells growing on glucose medium. For phosphorylation and dephosphorylation reaction, there are no experimentally measured rate constants. Barik *et al.* assigned values to these rate constants so that their model compared well with the observations of Di Talia *et al.* [38], and we have done the same in assigning values to γ , σ and the ω 's in Eqs 11 and 12. (S1 Table specifies four additional parameter values needed for the MultiP model.)

In both models, initial conditions are set as follows: $Cln3 = Clb5 = SBF = 0$, and initial conditions for all other variables are set at their steady state levels (see Table 2 for the SCM and S2 Table for the MultiP model). In the MultiP model, at the beginning of the simulation, all Whi5 is in the unphosphorylated form and all SBF is complexed with Whi5. In the SCM, at the beginning of the simulation, all Whi5 is in the active form and all SBF is complexed with active Whi5.

5. Stochastic version of SCM

Deterministic models are usually sufficient to predict the average behavior of a population of cells. However, at the level of individual cells, molecular regulatory networks operate under noisy conditions. A major source of noise inside cells are fluctuations of the numbers of molecules of biochemical species undergoing random events of synthesis and degradation. These inevitable fluctuations are referred to as “molecular noise”. Under the influence of such noise, the number of molecules, N , of a biochemical species fluctuates around the value predicted by the deterministic model. For a simple synthesis-degradation process, the variance of these fluctuations is equal to the mean value, $\langle N \rangle$, of the number of molecules [39]. Hence, the coefficient of variation ($CV = \text{standard deviation}/\text{mean}$) of the number of molecules is expected to be

Table 1. Parameter values for the standard component model of the START transition.

Parameter	Description	Value
$k_{a,g}$	Rate constant for association of SBF to <i>CLBS</i> promoter	$0.25 \text{ fL molec}^{-1} \text{ min}^{-1}$
$k_{d,bf}$	Rate constant for degradation of SBF	0.01 min^{-1}
$k_{d,bS}$	Rate constant for degradation of ClbS protein	0.1 min^{-1}
$k_{d,g}$	Rate constant for dissociation of SBF from <i>CLBS</i> promoter	12 min^{-1}
$k_{d,hi5}$	Rate constant for degradation of Hi5 phosphatase	0.01 min^{-1}
$k_{d,i5}$	Rate constant for degradation of Whi5	0.01 min^{-1}
$k_{d,mbS}$	Rate constant for degradation of <i>CLBS</i> mRNA	0.25 min^{-1}
$k_{d,mhi5}$	Rate constant for degradation of <i>HI5</i> mRNA	0.7 min^{-1}
$k_{d,mi5}$	Rate constant for degradation of <i>WHI5</i> mRNA	0.7 min^{-1}
$k_{d,mn3}$	Rate constant for degradation of <i>CLN3</i> mRNA	1 min^{-1}
$k_{d,n3}$	Rate constant for degradation of Cln3 protein	0.14 min^{-1}
$k_{s,bf}$	Rate constant for synthesis of SBF	$1.53 \text{ molec fL}^{-1} \text{ min}^{-1}$
$k_{s,bS}$	Rate constant for synthesis of ClbS protein	$0.3 \text{ fL}^{-1} \text{ min}^{-1}$
$k_{s,hi5}$	Rate constant for synthesis of Hi5 phosphatase	$0.1275 \text{ fL}^{-1} \text{ min}^{-1}$
$k_{s,i5}$	Rate constant for synthesis of Whi5 protein	$0.715 \text{ fL}^{-1} \text{ min}^{-1}$
$k_{s,mbS}$	Rate constant for synthesis of <i>CLBS</i> mRNA	$11.5 \text{ molec min}^{-1}$
$k_{s,mhi5}$	Rate constant for synthesis of <i>HI5</i> mRNA	7 molec min^{-1}
$k_{s,mi5}$	Rate constant for synthesis of <i>WHI5</i> mRNA	$5.25 \text{ molec min}^{-1}$
$k_{s,mn3}$	Rate constant for synthesis of <i>CLN3</i> mRNA	$7.5 \text{ molec min}^{-1}$
$k_{s,n3}$	Rate constant for synthesis of Cln3 protein	$0.0024 \text{ fL}^{-2} \text{ min}^{-1}$
$\langle m_{\text{min},bS} \rangle$	Minimum number of <i>CLBS</i> mRNA molecules	1 molec
$\langle m_{\text{min},hi5} \rangle$	Minimum number of <i>HI5</i> mRNA molecules	0
$\langle m_{\text{min},i5} \rangle$	Minimum number of <i>WHI5</i> mRNA molecules	0
$\langle m_{\text{min},n3} \rangle$	Minimum number of <i>CLN3</i> mRNA molecules	0
γ	Rate constant for Whi5 dephosphorylation	0.15 min^{-1}
μ	Specific growth rate of cells	0.007 min^{-1}
σ	Steepness of soft-Heaviside function	0.1
$\omega_{dp,i5}$	Interaction coeff for dephos'n of Whi5 by Hi5 phos'tase	$0.12 \text{ fL molec}^{-1}$
$\omega_{p,i5}$	Interaction coeff for phos'n of Whi5 by Cln3-dep kinase	$6.2 \text{ fL molec}^{-1}$
$\omega'_{p,i5}$	Interaction coeff for phos'n of Whi5 by ClbS-dep kinase	$0.33 \text{ fL molec}^{-1}$

doi:10.1371/journal.pone.0153738.t001

Table 2. Initial conditions for simulations of the standard component model of the START transition in Figs 3 and 5.

Variable	Number	Concentration
<i>ClbS</i>	0	0 nM
<i>Cln3</i>	0	0 nM
<i>Hi5</i>	1275	213 nM
<i>SBF_T</i>	1530	255 nM
<i>Whi5_A</i>	5363	894 nM
<i>Whi5_T</i>	5363	894 nM
<i>V</i>	10 fL	

doi:10.1371/journal.pone.0153738.t002

$1/\sqrt{\langle N \rangle}$, becoming proportionally larger as the mean number of molecules becomes smaller. For yeast cells, which carry only a few copies of some macromolecules (e.g., mRNA species), the fluctuations are potentially large.

To adapt an SCM for stochastic simulations, we add Langevin-type fluctuations to our equations for class-1 variables:

$$\frac{\Delta X_i}{\Delta t} = A_i - B_i \cdot X_i + \underbrace{\sqrt{A_i + B_i \cdot X_i} \cdot \frac{\zeta_1(t)}{\sqrt{\Delta t}}}_{\text{Protein noise}} + X_i \underbrace{\sqrt{2B_i \cdot \frac{1}{\langle m_i \rangle} \cdot \frac{B_i}{B_i + k_{dm}} \cdot \frac{\zeta_2(t)}{\sqrt{\Delta t}}}}_{\text{mRNA-inherited noise}}. \quad (17)$$

In this equation, molecular noise is attributed to random fluctuations at two levels: protein and mRNA. Fluctuations at the protein level are described by the chemical Langevin approximation [40]. A_i and B_i represent the protein synthesis and degradation rates as described in Eqs 2 and 3, respectively. $\zeta_1(t)$ and $\zeta_2(t)$ are independent random variables, each chosen from a normal distribution $N(0, 1)$ with mean = 0 and standard deviation = 1. Δt is the step size of the numerical integration. The last term in Eq 17 represents noise at the protein level inherited from fluctuations in mRNA molecules, and we next explain the origin of this term.

Since the number of mRNA molecules in a cell is typically much less than the numbers of protein molecules encoded by the mRNA, stochastic effects arising from mRNA fluctuations could contribute significantly to fluctuations in protein abundance. Instead of explicitly including mRNA dynamics in our SCM, as done in the Barik *et al.* model [27], we take an alternative approach. Pedraza and Paulsson [39] have shown that the square of the CV of protein numbers caused by mRNA fluctuations (at steady state) follows the equation

$$CV^2_{\text{mRNA-inherited noise}} = \frac{1}{\langle m \rangle} \cdot \frac{\tau_m}{\tau_m + \tau_p}, \quad (18)$$

Where $\langle m \rangle$ is the average number of mRNA molecules at steady state, and τ_m and τ_p are half-lives of mRNAs and proteins, respectively. The last term of Eq 17 was derived to approximate the CV^2 predicted by Eq 18 under steady state conditions for the protein and mRNA levels (see S2 Text for the derivation). In Eq 17, k_{dm} is the rate constant for mRNA degradation; so the term $B_i/(B_i + k_{dm})$ is equal to $\tau_m/(\tau_m + \tau_p)$ in Eq 18.

There is still a problem with the mRNA noise term in Eq 17. When $\langle m_i \rangle$ is small (e.g., the case of a low level of the transcription factor SBF in Eq 10), the Langevin approximation breaks down and the noise term becomes very large. To avoid this, we replace $\langle m_i \rangle$ with $\langle m_i \rangle + \langle m_{\min,i} \rangle$ in our simulation, where $\langle m_{\min,i} \rangle$ is assumed to be a minimum number of mRNA molecules always present in the cell. Eq 17 then becomes

$$\begin{aligned} \frac{\Delta X_i}{\Delta t} = & A_i - B_i \cdot X_i + \underbrace{\sqrt{A_i + B_i \cdot X_i} \cdot \frac{\zeta_1(t)}{\sqrt{\Delta t}}}_{\text{Protein noise}} \\ & + X_i \underbrace{\sqrt{2B_i \frac{1}{\langle m_i \rangle + \langle m_{\min,i} \rangle} \cdot \frac{B_i}{B_i + k_{dm}} \cdot \frac{\zeta_2(t)}{\sqrt{\Delta t}}}}_{\text{mRNA-inherited noise}}, \end{aligned} \quad (19)$$

We treat $\langle m_{\min,i} \rangle$ as a parameter, and its value may vary from one mRNA species to another.

We do not incorporate protein and mRNA noise terms into variables of classes 2 and 3. We assume that protein phosphorylation and dephosphorylation reactions and the association and

dissociation of protein complexes occur fast enough to bring any fluctuations quickly back to the average dynamics.

To create a stochastic SCM for the budding yeast *START* transition, we modify the equations of class-1 variables by adding Langevin-type noise terms, as in Eq 19. For example, the stochastic equation for *Cln3* is:

$$\begin{aligned} \frac{\Delta Cln3}{\Delta t} &= A_{n3} - B_{n3} \cdot Cln3 + \sqrt{A_{n3} + B_{n3} \cdot Cln3} \cdot \frac{\zeta_1(t)}{\sqrt{\Delta t}} \\ &+ Cln3 \sqrt{2B_{n3} \frac{1}{\langle m_{n3} \rangle + \langle m_{min,n3} \rangle} \cdot \frac{B_{n3}}{B_{n3} + k_{d,mn3}}} \cdot \frac{\zeta_2(t)}{\sqrt{\Delta t}} \\ A_{n3} &= k_{s,n3} \cdot V^2 \cdot \frac{k_{s,mn3}}{k_{d,mn3}} \\ B_{n3} &= k_{d,n3} \\ \langle m_{n3} \rangle &= \frac{k_{s,mn3}}{k_{d,mn3}}, \end{aligned} \tag{20}$$

where A_{n3} and B_{n3} represent the synthesis and degradation rates of *Cln3* protein, and $\langle m_{n3} \rangle$ is the average number of *CLN3* mRNA molecules calculated at steady state. $\langle m_{min,n3} \rangle$ is a parameter representing the minimum number of *CLN3* mRNA molecules present in the cell. The full list of stochastic equations is given in S3 Text.

Barik *et al.* [27] used Gillespie's SSA to simulate all chemical reactions in their stochastic model. They assumed that hyper-phosphorylation of *Whi5* corresponds to its nuclear export (as an indication of the *START* transition). Their model accurately predicted the timing of the transition and its dependence on cell size at birth, when compared with experimental observations of Di Talia *et al.* [38].

In the next section, we compare deterministic and stochastic simulations of our SCM to deterministic and stochastic simulations of the MultiP model in S1 Text, and we show that the SCM, a model considerably less complex than MultiP, accounts for most of the dynamic properties of the system.

6. Comparisons of the Start model simulations

To validate our approach, we compare qualitative and quantitative aspects of the SCM to the MultiP model. Fig 2 shows the one-parameter bifurcation curves for both models, in which we plot the steady-state number of *Clb5* molecules as a function of cell volume (V) as the bifurcation parameter. Both models exhibit bistability within a range of V from ~6 fL to ~30 fL. Hence, both models agree on cell size at the *START* transition (~30 fL) for wild-type cells. New-born cells in G_1 phase of the cell cycle are captured by the stable steady state with *Clb5* level very low. They must grow to a size of ~30 fL, before the lower stable steady state disappears at a saddle-node bifurcation point. For $V > 30$ fL, the number of *Clb5* molecules rises rapidly to the high steady-state level, corresponding to the *START* transition. In S2 Fig, we use two-parameter bifurcation diagrams to show how the SCM and the MultiP model behave when the synthesis rates of *Cln3* and *Clb5* are varied at various (fixed) cell size.

Next we compare time-series dynamics of the two models in their deterministic formulations (i.e., simulations of the nonlinear ODEs). In Fig 3, we show simulations of a cell that starts with $V = 10$ fL at $t = 0$. The two models show very similar time courses for the control proteins. As in the multisite phosphorylation paper [27], we mark the *START* transition as the time when the concentration of active SBF increases above 15 nM and the G_1/S transition as the time

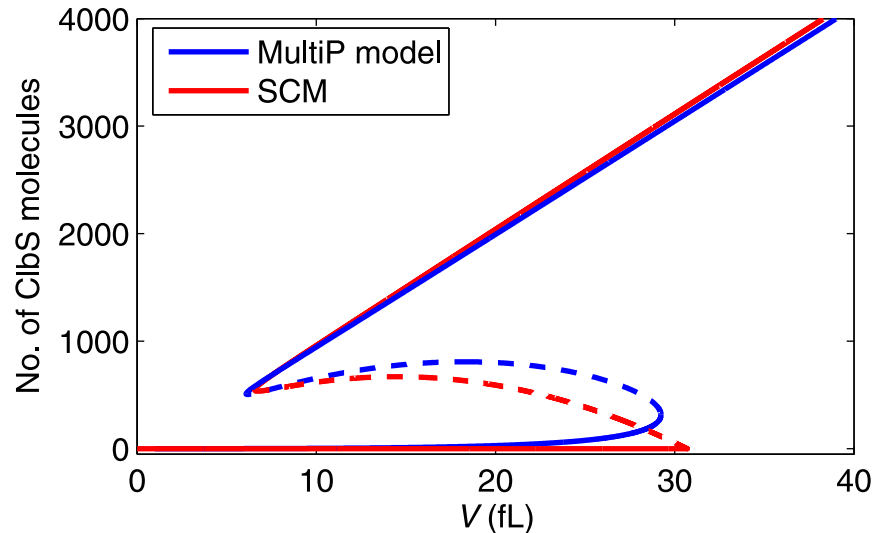


Fig 2. One-parameter bifurcation diagram. The steady-state number of ClbS molecules is plotted as a function of (fixed) cell volume. Solid line: stable steady states; dashed line: unstable steady states; blue lines: multisite phosphorylation (MultiP) model; red lines: standard component model (SCM). Both models exhibit a region of bistability between $V \approx 6$ fL and $V \approx 30$ fL. The right bifurcation point (at $V \approx 30$ fL) corresponds to the threshold size for the S_{START} transition.

doi:10.1371/journal.pone.0153738.g002

when ClbS concentration increases above 37.5 nM. Concentration in nM is calculated from molecule number N and volume V in fL by the formula

$$\text{concentration (nM)} = \frac{\text{number of molecules}}{N_A (\text{mol}^{-1}) \times V (\text{fL})} \times 10^9 \frac{\text{nmol}}{\text{mol}} \times 10^{15} \frac{\text{fL}}{\text{L}} = \frac{N}{0.6 V (\text{fL})}$$

where N_A is Avogadro's number, 6.02×10^{23} .

Since it is well known that the smaller is cell size at birth the longer is the time to initiate bud formation and to enter S phase, we measure the durations from birth ($t = 0$) to the S_{START} transition (T_1) and to the G_1/S transition (T_{G_1}) for various values of initial volume, V_0 . In Fig 4, we plot T_1 and T_{G_1} as functions of initial cell size. (The left-most bars of the figure correspond to the time-series simulations in Fig 3). The results show that the SCM is quantitatively comparable to the more complex MultiP model. The figure also shows that T_1 and T_{G_1} decrease as birth size increases, consistent with experimental observations [38]. The gap between S_{START} and the G_1/S transition, $T_2 = T_{G_1} - T_1$, is small in both models (S3 Fig) and nearly independent of birth size [38].

Next we study stochastic properties of the models. The MultiP model is simulated by SSA [13] while the SCM is simulated by the CLE approximation described above. S4 Fig compares the steady-state distributions of Cln3, SBF and ClbS at fixed volume for the MultiP model and the SCM. Fig 5 shows envelopes of sample trajectories from stochastic simulations of both models, starting with $V = 10$ fL at $t = 0$. Distributions of T_1 and T_{G_1} can be computed for the stochastic models as functions of V_0 . For each value of V_0 , we do 100 independent simulations of each model and compute the average values and standard deviations of T_1 and T_{G_1} . The average values show similar patterns to the deterministic simulations in Fig 4 (see S5 Fig). The coefficient of variation (CV) is shown in Fig 6 and the distributions of T_1 and T_{G_1} are shown in S6 Fig. The results show that the noise intensities of both models agree well at small V_0 but not at large V_0 (red and green bars in Fig 6). Our SCM without mRNA fluctuations (i.e., discarding the mRNA-inherited noise term from the equations) shows less intensity of noise (blue bars in

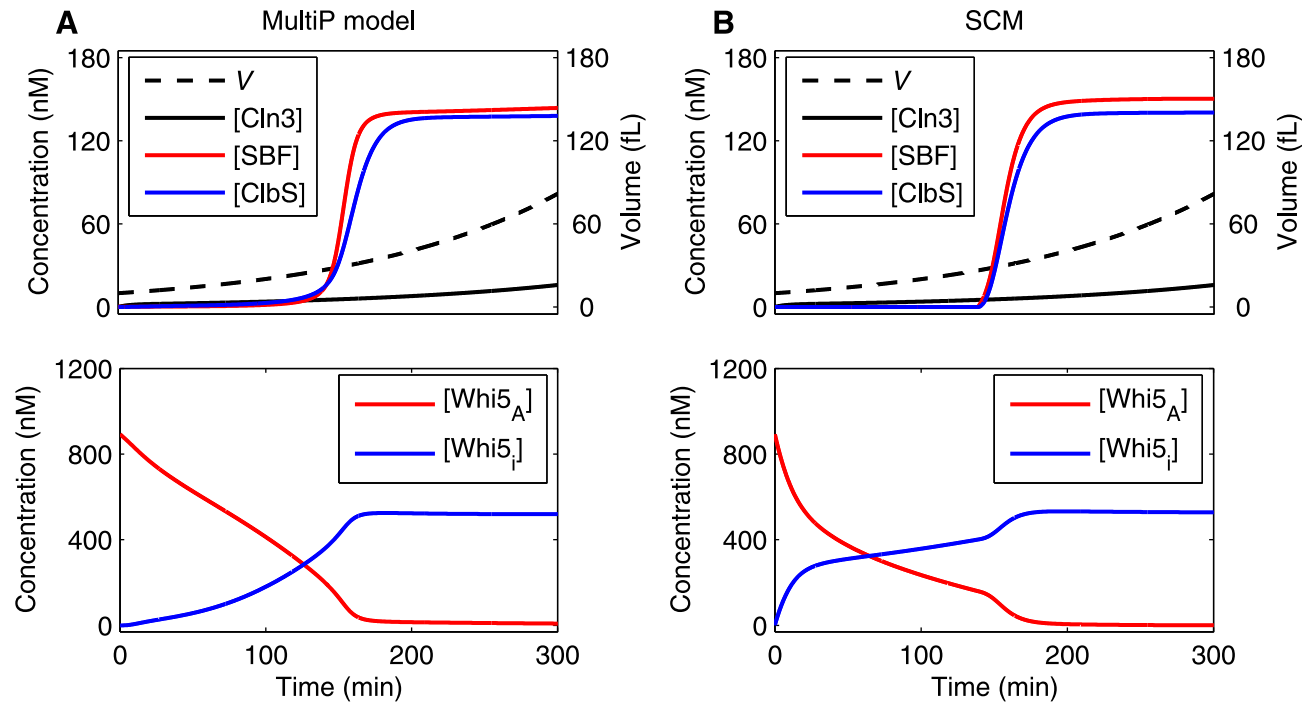


Fig 3. Deterministic trajectories simulated by the MultiP model and the SCM of the Start transition. Both models are simulated for 300 min, starting with $V = 10$ fL at $t = 0$. Initial conditions for the SCM are specified in Table 2 and for the MultiP model in S2 Table. In these panels we plot concentration (in nM), which is calculated from molecule number and volume (in fL) by the formula “concentration” = “number”/($0.6 \times$ “volume in fL”). In the MultiP model, $Whi5_A = Whi5 + Whi5P_1 + Whi5P_2 + Cmp + CmpP_1 + CmpP_2$. In both models, $Whi5_I = Whi5_T - Whi5_A$. The changes in $Whi5_A$ and $Whi5_I$ over the first 100 min are quite different in the two models because their descriptions of the $Whi5$ activation process are quite different. Nonetheless, they predict similar timing for the cell cycle transitions. We presume that the $START$ and G_1/S transitions occur when $[SBF] = 15$ nM and $[ClbS] = 37.5$ nM, respectively. (These values are 50% of the maximum concentrations from the original MultiP model [27], not 50% of the final concentrations shown in this figure). The MultiP model (left panels) executes the $START$ and G_1/S transitions at $t = 142$ min and $t = 152$ min, respectively. The SCM (right panels) executes the $START$ and G_1/S transitions at $t = 145$ min and $t = 153$ min, respectively.

doi:10.1371/journal.pone.0153738.g003

Fig 6), indicating that mRNA fluctuations are important. By expanding the SCM to include mRNA synthesis and degradation explicitly and simulating mRNA fluctuations using CLEs (see equations in S4 Text), we obtained much better agreement with the fully stochastic MultiP model (Fig 7), but at a cost of considerably more complexity.

With this simple model of the $START$ transition in budding yeast, we have shown that the SCM approach can capture essential dynamical features of a complex control network in quantitative detail. Encouraged by these results, we built an SCM of the full network of molecular controls of the budding yeast cell cycle, as described in the next section.

7. An SCM for the budding yeast cell cycle control system

Our cell cycle model (Fig 8) is based on the interaction network proposed in [41] with some modifications in the $START$ transition (by adding the inhibition of SBF by $Whi5$) and mitotic exit (by adding the stimulatory effects of Polo kinase and separase Esp1 on Cdc14 release), according to the models proposed in [36] and [42], respectively. In the model of Chen *et al.* [41] (Chen-2004, hereafter), each component is represented in terms of a concentration that has been scaled to a dimensionless number, called its normalized concentration, $[\]_n$. Cell volume, V_n , is also dimensionless. In order to compare SCM simulations directly to Chen-2004, we switch from numbers of molecules to normalized concentrations, using the “characteristic

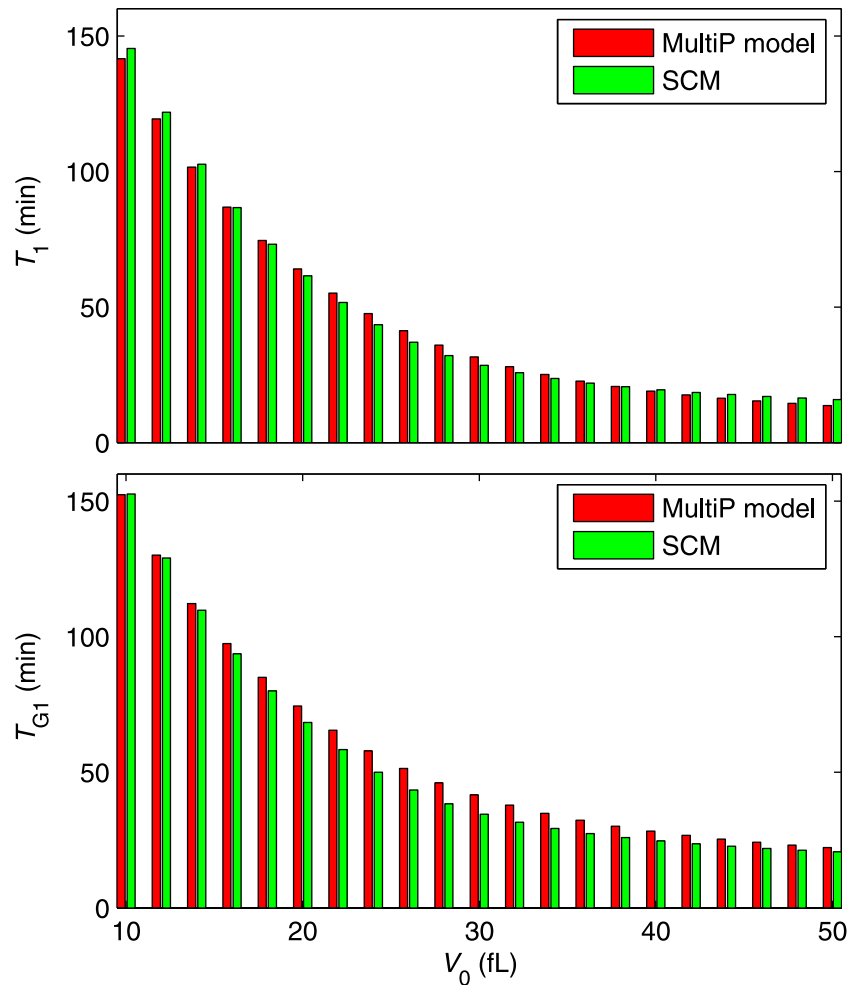


Fig 4. Deterministic simulations of the relation between initial cell size (V_0) and cell age at the Start transition (T_1) (upper panel) and cell age at the G_1/S transition (T_{G1}) (lower panel) for the Start models. Red bars: MultiP model; green bars: SCM. The left-most bars of the figure correspond to the time-series simulations in Fig 3.

doi:10.1371/journal.pone.0153738.g004

concentrations” listed in Table 3. To be more specific, $[S]_n = [S]/c_S = N_S/(0.6 V \cdot c_S)$, where $[S]$ = concentration of species S in nM, c_S = characteristic concentration of S in nM, N_S = number of S molecules in volume V (in fL), and $V = V_n c_{vol}$.

In budding yeast, as in all eukaryotes, cyclin/Cdk complexes are the main regulators of cycle progression. The kinase subunit, Cdc28, being far more abundant than all cyclin proteins, is always available to bind to any cyclins present in the cell [31]. Therefore, we use concentrations of cyclins to indicate the activities of cyclin/Cdc28 complexes (neglecting Cdc28 itself in the model). As in previous models, components that have similar functions are treated as single variables; for instance, “SBF” stands for SBF and MBF, “Cln2” for Cln1 and Cln2, “Clb2” for Clb1 and Clb2, “Clb5” for Clb5 and Clb6, and “CKI” for Sic1 and Cdc6.

For the cell cycle control system, class-1 variables include proteins whose concentrations change slowly over time due to the activities of transcription factors and proteolytic enzymes. This class includes, for example, the total concentrations of cyclin proteins (Cln2, Cln3, Clb2, and Clb5) and the total concentration of the stoichiometric inhibitor CKI. The synthesis of Cln2 and Clb5 is regulated by the transcription factor SBF, the synthesis of Clb2 is regulated by

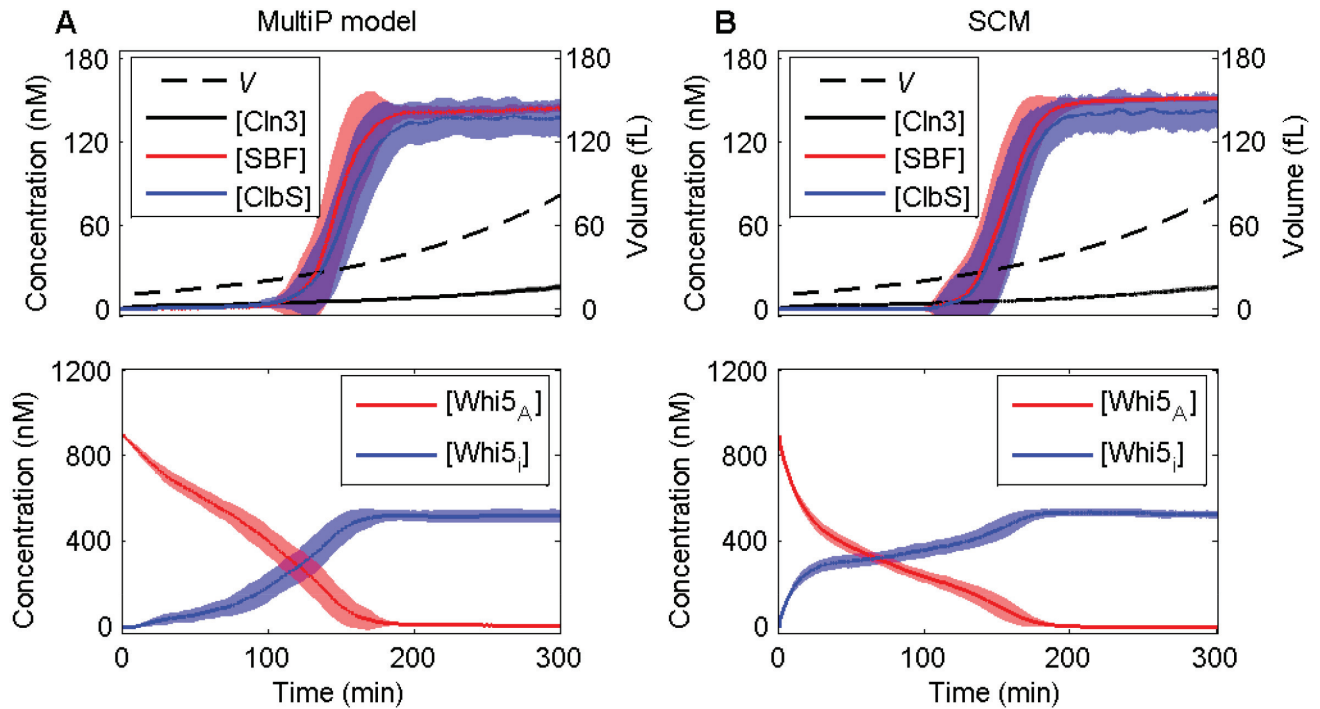


Fig 5. Stochastic trajectories generated by the MultiP model and the SCM of the Start transition. Means (lines) and standard deviations (shadows) calculated from 100 independent trajectories are shown for each model, starting with $V = 10$ fL at $t = 0$. Initial conditions for the SCM are specified in Table 2 and for the MultiP model in S2 Table. As in Fig 3 we plot “concentration in nM” = “number of molecules”/($0.6 \times$ “volume in fL”). The MultiP model is simulated by Gillespie’s SSA and the SCM is simulated by the chemical Langevin approach described in the text.

doi:10.1371/journal.pone.0153738.g005

the transcription factor Mcm1, and the synthesis of CKI is controlled by the transcription factor Swi5. The degradation of Clb2 and Clb5 is regulated by the proteolytic factors Cdc20 and Cdh1 in association with an E3 ubiquitin ligase called the Anaphase Promoting Complex (APC).

The properties of many cell cycle-control proteins can be regulated by phosphorylation and dephosphorylation. For instance, phosphorylated Whi5 is a less potent inhibitor of SBF, and phosphorylated CKI is more susceptible to proteolysis. We use class-2 variables to represent the fractions of these proteins that are in “active” forms. The regulation of protein activity by phosphorylation and dephosphorylation is believed to be essential for the bistable switches that govern cell cycle transitions [6, 27, 36, 41, 43–45]. Class-2 variables capture the nonlinear behavior of these reactions in terms of the “soft-Heaviside” functions built into the SCM formulation.

Class-3 variables represent the free forms of proteins that form tight complexes with stoichiometric binding partners. For example, both Clb5 and Clb2 are inhibited by binding to CKI, as is Cdc14 inhibited by binding to Net1. In these cases, the “max” function employed by SCMs is a reasonable approximation because stoichiometric inhibitors usually bind strongly and rapidly to their partners. This strong-binding assumption is part of the original ODE model as well [41].

In Fig 8 we have divided the regulatory network into three modules (START, S/G₂/M, and EXIT), which provides a useful framework for constructing the SCM. In Table 3 we classify the regulatory proteins into the three classes of SCM variables, and in Table 4 we translate Fig 8 into the differential and algebraic equations that define the dynamics of the network according to the SCM approach.

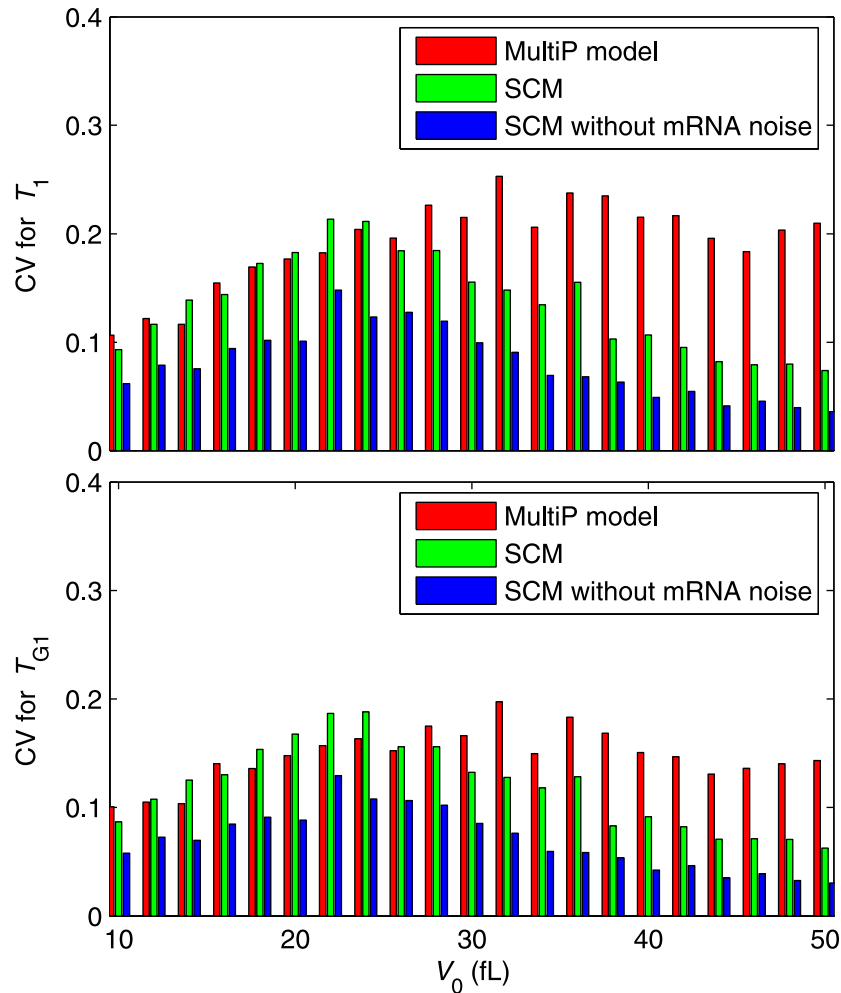


Fig 6. Stochastic simulations of T_1 and T_{G1} for the Start models. As in Fig 4, we compute the times from birth ($t = 0, V = V_0$) to the T_{START} transition (T_1 , when $[SBF] = 15$ nM for the first time; upper panel) and to the G_1/S transition (T_{G1} , when $[ClbS] = 37.5$ nM for the first time; lower panel). For each model we compute 100 stochastic trajectories and calculate the mean and standard deviation of the time to the event. The mean times agree well with the deterministic simulations in Fig 4. Here we plot the coefficient of variation (CV = standard deviation/mean) of the times, in order to judge how well stochastic CLE simulations of the SCM (green bars) compare with SSA simulations of the MultiP model (red bars). Clearly the SCM underestimates the variability of the transitions at large birth size. Removing mRNA noise from the SCM (blue bars) makes matters worse, as expected.

doi:10.1371/journal.pone.0153738.g006

Formulation of the Start module. Components involved in the T_{START} transition (for a review, see [46]) are governed by Eqs 22–30. The molecular mechanism of the T_{START} transition considered here (Fig 8A) is more complex than the test case (Fig 1C) considered earlier. First, instead of lumping Cln2 and Clb5 into one variable (ClbS), we separate them (Eqs 24 and 31) because they are controlled differently: unlike Clb5, Cln2 is not inhibited by CKI [47] and not degraded by Cdc20 [48]. Second, we add a component Bck2 (Eq 23), which is known to activate SBF in parallel to Cln3 [49, 50]. Third, the dephosphorylation of Whi5 by Hi5, an unknown phosphatase, is considered as a background dephosphorylation ($\omega_{dp,whi5}$) since we assume that the concentration of Hi5 is always constant. Finally, Cdc14, a component that is active in late mitosis, also contributes to dephosphorylation of Whi5 during mitotic exit [51].

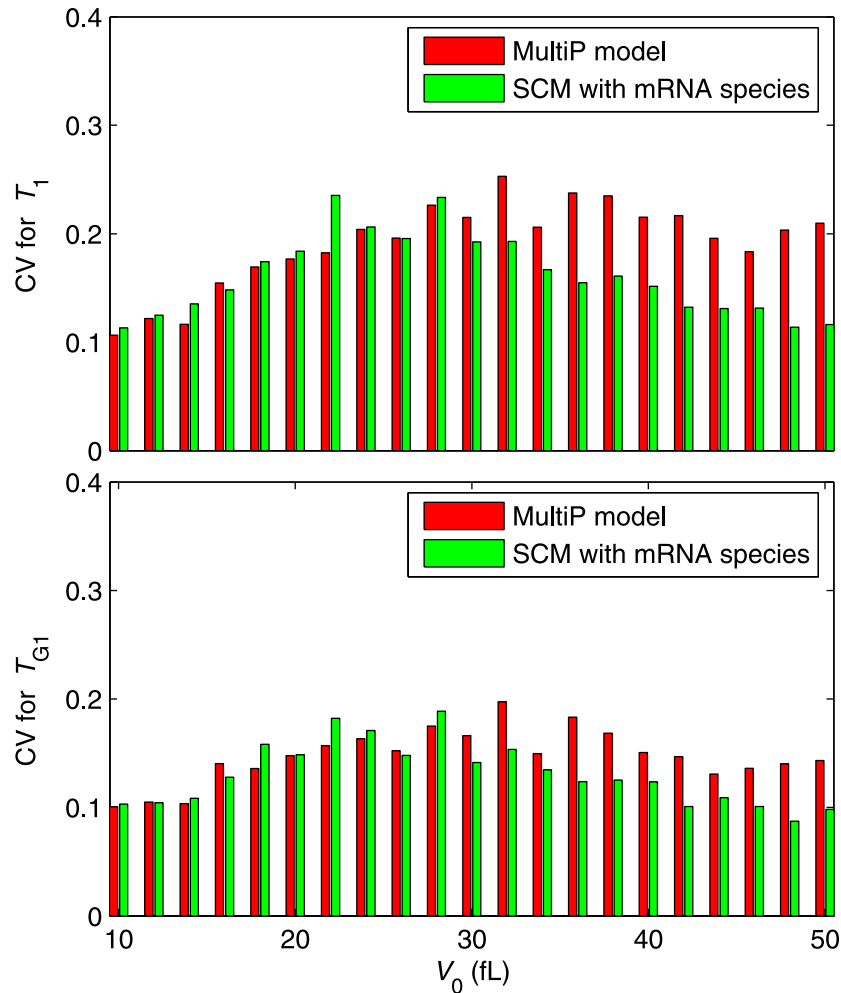


Fig 7. Stochastic simulations of T_1 and T_{G1} for the Start SCM with explicit account of fluctuating mRNA species. As in Fig 6, except now we have added synthesis and degradation of mRNA species explicitly to the SCM. The remaining discrepancies are attributable in part to differences between the models and in part to simulating mRNA noise by CLE rather than SSA.

doi:10.1371/journal.pone.0153738.g007

Concentrations of Cln3, Bck2, and Cln2 are controlled by synthesis and degradation and described by class-1 variables (Table 4, Eqs 22, 23 and 24, respectively). The G_1/S transition ($START$) in budding yeast is known to be sensitively dependent on cell size [33], and $START$ is known to be strongly dependent on the expression of *CLN3* and *BCK2* genes [31, 34, 52]. To account for these facts, we assume that the synthesis rates of Cln3 and Bck2 proteins are proportional to cell size, V . (This assumption was also made in Chen-2004 [41] and in the stochastic model of Barik *et al.* [27].) The production of Cln2 is controlled by the SBF transcription factor.

The activity of SBF is controlled by binding to an inhibitor, Whi5 [29, 30], and by phosphorylation (inactivation) by Clb2 [53, 54]; see Table 4, Eqs 27, 28 and 29. In order to bind to SBF, Whi5 must also be in its unphosphorylated form. Therefore, functional SBF, $[SBF]_n$ in Eq 29, is the amount of unphosphorylated SBF, denoted $[SBF_A]_n$, that is not bound to unphosphorylated Whi5, denoted $[Whi5_A]_n$. For simplicity, we assume that phosphorylated SBF does not bind to unphosphorylated Whi5.

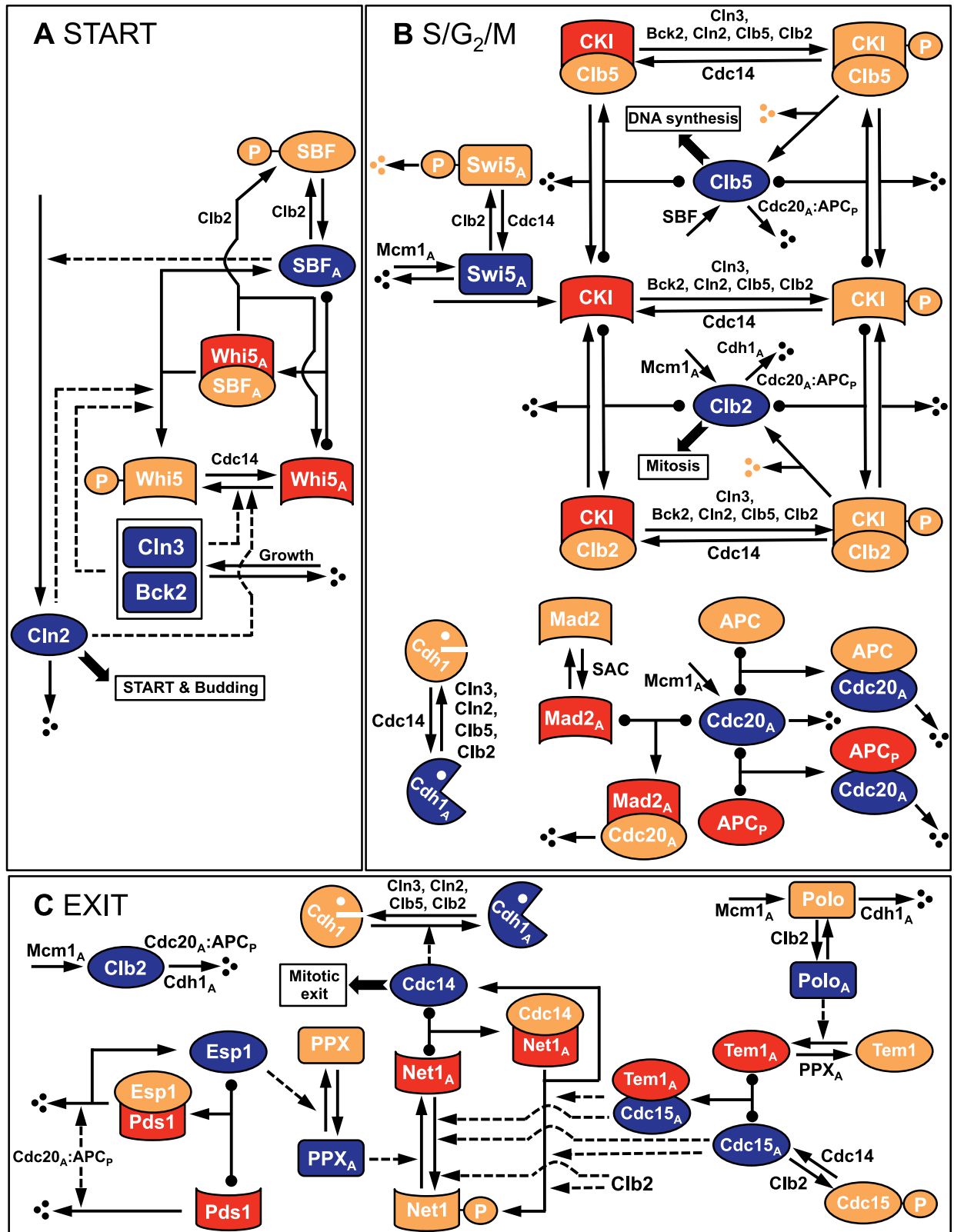


Fig 8. Wiring diagram of the full cell cycle control network in budding yeast. The network consists of three major modules: START, S/G₂/M, and EXIT. Red and blue icons: active forms of components; orange icons: inactive forms. Solid lines: chemical reactions

(synthesis and degradation, phosphorylation and dephosphorylation, association and dissociation); dashed lines: activatory or inhibitory influences of components on chemical reactions. T-shaped reaction arrows with black circles on the reactants side of the arrow indicate reversible association of two proteins to form a complex. T-shaped arrows without black circles represent irreversible reactions. Not all reactions are shown on this figure; see the equations in Table 4 for complete details.

doi:10.1371/journal.pone.0153738.g008

In early G₁, Clb2 level is low, so SBF is unphosphorylated, but it is not active because Whi5 is also unphosphorylated, and Whi5_A binds rapidly and strongly to SBF_A [29, 30]. As the cell grows, Cln3 and Bck2 accumulate and phosphorylate Whi5. Phosphorylated Whi5 dissociates from SBF and translocates from nucleus to cytoplasm [29, 30], leaving SBF free to do its job as a

Table 3. Variables, initial values and characteristic concentrations for the standard component model of the full cell cycle control system.

Variable*	Description	Class	Initial Value	Characteristic Concentration
[APC _P] _n	Active (phosphorylated) form of APC	2	0.1216	150 nM
[Bck2] _n	Total concentration of Bck2	1	0.0308	40 nM
[BUD] _n	Progress to bud emergence	-	0.0488	-
[Cdc14] _n	Active form of Cdc14 phosphatase	3	1.8914	18 nM
[Cdc15 _A] _n	Active form of Cdc15 kinase	2	0.9823	8 nM
[Cdc20 _T] _n	Total Cdc20, an APC partner	1	1.2422	150 nM
[Cdc20 _A] _n	Active form of Cdc20	3	0.7925	
[Cdc20 _A :APC _P] _n	Complex between Cdc20 _A and APC _P	3	0.1216	
[Cdc20 _A :APC] _n	Complex between Cdc20 _A and APC	3	0.6710	
[Cdh1 _A] _n	Active form of Cdh1, an APC partner	2	0.9574	150 nM
[CKI _P] _n	Phosphorylated forms of Sic1 & Cdc6	2	0	
[CKI _T] _n	Total cyclin inhibitors Sic1 & Cdc6	1	0.4012	40 nM
[Clb2] _n	Active forms of cyclins Clb1 & Clb2	3	0.1011	
[Clb2 _T] _n	Total cyclins Clb1 & Clb2	1	0.2687	40 nM
[Clb5] _n	Active forms of cyclins Clb5 & Clb6	3	0.1412	
[Clb5 _T] _n	Total cyclins Clb5 & Clb6	1	0.3752	40 nM
[Cln2] _n	Total cyclins Cln1 & Cln2	1	0.1343	40 nM
[Cln3] _n	Total cyclin Cln3	1	0.0757	40 nM
[Esp1] _n	Active form of separase	3	0.4706	3.3 nM
[Mad2 _A] _n	Active form of Mad2, a spindle assembly checkpoint protein	2	0.4497	150 nM
[Mcm1 _A] _n	Active form of transcr factor for Clb2	2	0	100 nM
[Net1 _A] _n	Active form of inhibitor of Cdc14	2	0.1086	18 nM
[ORI] _n	Progress to DNA synthesis	-	0.0710	-
[Pds1 _T] _n	Securin, an inhibitor of Esp1	1	0.0294	3.3 nM
[Polo _A] _n	Active form of Cdc5 kinase	2	0.2073	
[Polo _T] _n	Total Cdc5 kinase	1	0.2915	100 nM
[PPX _A] _n	Active form of a phosphatase	2	0.0128	100 nM
[SBF] _n	Active (free) form of SBF transcription factor	3	0	22 nM
[SBF _A] _n	Unphosphorylated form of SBF	2	0.6560	
[SPN] _n	Progress to spindle assembly	-	0.0389	
[Swi5 _A] _n	Active form of Swi5	2	0.6333	
[Swi5 _T] _n	Total Swi5, transcription factor of CKI	1	0.6333	57.5 nM
[Tem1 _A] _n	Active form of Tem1, a G-protein kinase	2	0.8592	8 nM
[Tem1 _A :Cdc15 _A] _n	Complex between Tem1 _A and Cdc15 _A	3	0.8592	
[Whi5 _A] _n	Active (unphosphorylated) form of Whi5	2	1.7238	22 nM
V _n	Cell size (in normalized volume unit)	-	1.1460	28 fL

* [. .]_n refers to normalized (dimensionless) concentration variables

doi:10.1371/journal.pone.0153738.t003

Table 4. Equations for the standard component model of the full cell cycle system.

Cell Growth	
$\frac{dV_n}{dt} = \mu \cdot V_n$	(21)
START Module	
$\frac{d[Cln3]_n}{dt} = k_{s,cln3} \cdot \frac{D_{cln3} \cdot V_n}{J_{cln3} + D_{cln3} \cdot V_n} - k_{d,cln3} \cdot [Cln3]_n$	(22)
$\frac{d[Bck2]_n}{dt} = k_{s,bck2} \cdot V_n - k_{d,bck2} \cdot [Bck2]_n$	(23)
$\frac{d[Cln2]_n}{dt} = k_{s,cln2} + k_{s,cln2,bf} \cdot [SBF]_n - k_{d,cln2} \cdot [Cln2]_n$	(24)
$\frac{d[Whi5_A]_n}{dt} = \gamma \cdot ([Whi5_T]_n \cdot H(\sigma \cdot W_{Whi5}) - [Whi5_A]_n)$	(25)
$W_{Whi5} = \omega_{dp,whi5} + \omega_{dp,whi5,14} \cdot [Cdc14]_n - \omega_{p,whi5,n3} \cdot [Cln3]_n - \omega_{p,whi5,k2} \cdot [Bck2]_n - \omega_{p,whi5,n2} \cdot [Cln2]_n - \omega_{p,whi5,b5} \cdot [Clb5]_n$	(26)
$\frac{d[SBF_A]_n}{dt} = \gamma \cdot ([SBF_T]_n \cdot H(\sigma \cdot W_{sbf}) - [SBF_A]_n)$	(27)
$W_{sbf} = \omega_{dp,sbf} - \omega_{p,sbf,b2} \cdot [Clb2]_n$	(28)
$[SBF]_n = \max(0, [SBF_A]_n - [Whi5_A]_n)$	(29)
$\frac{d[BUD]_n}{dt} = k_{s,bud,e} \cdot (e_{bud,n3} \cdot [Cln3]_n + e_{bud,n2} \cdot [Cln2]_n + e_{bud,b5} \cdot [Clb5]_n) - k_{d,bud} \cdot [BUD]_n$	(30)
S/G₂/M Module	
$\frac{d[Clb5_T]_n}{dt} = k_{s,clb5} + k_{s,clb5,bf} \cdot [SBF]_n - (k_{d,clb5} + k_{d,clb5,20} \cdot [Cdc20_A : APC_P]_n + k_{d,clb5,20,i} \cdot [Cdc20_A : ABC_P]_n) \cdot [Clb5_T]_n$	(31)
$\frac{d[Clb2_T]_n}{dt} = (k_{s,clb2} + k_{s,clb2,m1} \cdot [Mcm1_A]_n) \cdot V_n - (k_{d,clb2} + k_{d,clb2,20} \cdot [Cdc20_A : APC_P]_n + k_{d,clb2,20,i} \cdot [Cdc20_A : APC]_n + k_{d,clb2,h1} \cdot [Clb1_A]_n) \cdot [Clb2_T]_n$	(32)
$\frac{d[CKI_T]_n}{dt} = k_{s,cki} + k_{s,cki,swi5} \cdot [Swi5_A]_n - k_{d,cki} \cdot ([CKI_T]_n - [CKI_P]_n) - k_{d,ckip} \cdot [CKI_P]_n$	(33)
$\frac{d[CKI_P]_n}{dt} = \gamma \cdot ([CKI_T]_n \cdot H(\sigma \cdot W_{cki}) - [CKI_P]_n) - k_{d,ckip} \cdot [CKI_P]_n$	(34)
$W_{cki} = \omega_{p,cki,n3} \cdot [Cln3]_n + \omega_{p,cki,k2} \cdot [Bck2]_n + \omega_{p,cki,n2} \cdot [Cln2]_n + \omega_{p,cki,b5} \cdot [Clb5]_n + \omega_{p,cki,b2} \cdot [Clb2]_n - \omega_{dp,cki} - \omega_{dp,cki,14} \cdot [Cdc14]_n$	(35)
$[Clb5]_n = \max\left(0, \frac{[Clb5_T]_n}{[Clb5_T]_n + [Clb2_T]_n} \cdot ([Clb5_T]_n + [Clb2_T]_n - [CKI_T]_n)\right)$	(36)
$[Clb2]_n = \max\left(0, \frac{[Clb2_T]_n}{[Clb5_T]_n + [Clb2_T]_n} \cdot ([Clb5_T]_n + [Clb2_T]_n - [CKI_T]_n)\right)$	(37)
$\frac{d[Swi5_T]_n}{dt} = k_{s,swi5} + k_{s,swi5,m1} \cdot [Mcm1_A]_n - k_{d,swi5} \cdot [Swi5_T]_n$	(38)
$[Swi5_A]_n = [Swi5_T]_n \cdot H(\sigma \cdot W_{swi5})$	(39)
$W_{swi5} = \omega_{a,swi5,14} \cdot [Cdc14]_n - \omega_{i,swi5,b2} \cdot [Clb2]_n$	(40)
$\frac{d[ORI]_n}{dt} = k_{s,ori,e} \cdot (e_{ori,b5} \cdot [Clb5]_n + e_{ori,b2} \cdot [Clb2]_n) - k_{d,ori} \cdot [ORI]_n$	(41)
$\frac{d[Cdh1_A]_n}{dt} = \gamma \cdot ([Cdh1_T]_n \cdot H(\sigma \cdot W_{cdh1}) - [Cdh1_A]_n)$	(42)
$W_{cdh1} = \omega_{a,cdh1} + \omega_{a,cdh1,14} \cdot [Cdc14]_n - \omega_{i,cdh1,e} \cdot (\omega_{i,cdh1,n3} \cdot [Cln3]_n + \omega_{i,cdh1,n2} \cdot [Cln2]_n + \omega_{i,cdh1,b5} \cdot [Clb5]_n + \omega_{i,cdh1,b2} \cdot [Clb2]_n)$	(43)
$[Mcm1_A]_n = [Mcm1_T]_n \cdot H(\sigma \cdot W_{mcm1})$	(44)
$W_{mcm1} = \omega_{a,mcm1,b2} \cdot [Clb2]_n - \omega_{i,mcm1}$	(45)
$\frac{d[APC_P]_n}{dt} = \gamma_{apc} \cdot ([APC_T]_n \cdot H(\sigma \cdot W_{apc}) - [APC_P]_n)$	(46)
$W_{apc} = \omega_{a,apc,b2} \cdot [Clb2]_n - \omega_{i,apc}$	(47)
$\frac{d[Mad2_A]_n}{dt} = \gamma \cdot ([Mad2_T]_n \cdot H(\sigma \cdot W_{mad2}) - [Mad2_A]_n)$	(48)
$W_{mad2} = \omega_{a,mad2} \cdot B_{udna} \cdot (1 - B_{spc}) - \omega_{i,mad2}$	(49)
$\frac{d[SPN]_n}{dt} = k_{s,spn} \cdot Heav([Clb2]_n - J_{spn}) - k_{d,spn} \cdot [SPN]_n$	(50)
$\frac{d[Cdc20_T]_n}{dt} = k_{s,cdc20} + k_{s,cdc20,m1} \cdot [Mcm1_A]_n - k_{d,cdc20} \cdot [Cdc20_T]_n$	(51)
$[Cdc20_A]_n = \max(0, [Cdc20_T]_n - [Mad2_A]_n)$	(52)
$[Cdc20_A]_n = \min([Cdc20_A]_n, [APC_P]_n)$	(53)
$[Cdc20_A : APC]_n = \min([Cdc20_A]_n - [Cdc20_A : APC_P]_n, [APC_T]_n - [APC_P]_n)$	(54)

(Continued)

Table 4. (Continued)

EXIT MODULE	
$\frac{d[Pds1_T]_n}{dt} = k_{s,pds1} - (k_{s,pds1} + k_{d,pds1,20} \cdot [Cdc20_A : APC_P]_n + k_{d,pds1,20,i} \cdot [Cdc20_A : APC]_n \cdot [Pds1_T]_n$	(55)
$[Esp1]_n = \max(0, [Esp1_T]_n - [Pds1_T]_n$	(56)
$\frac{d[PPX_A]_n}{dt} = \gamma \cdot ([PPX_T]_n \cdot H(\sigma \cdot W_{ppx}) - [PPX_A]_n)$	(57)
$W_{ppx} = \omega_{a,ppx} - \omega_{i,ppx,p1} \cdot [Esp1]_n$	(58)
$\frac{d[Net1_A]_n}{dt} = \gamma \cdot ([Net1_T]_n \cdot H(\sigma_{net1} \cdot W_{net1}) - [Net1_A]_n)$	(59)
$W_{net1} = \omega_{dp,net1} + \omega_{dp,net1,14} \cdot [Cdc14]_n + \omega_{dp,net1,px} \cdot [PPX_A]_n - \omega_{p,net1,b2} \cdot [Clb2]_n - \omega_{p,net1,en} \cdot [Tem1_A : Cdc15_A]_n - \omega_{p,net1,15} \cdot ([Cdc15_A]_n : [Tem1_A : Cdc15_A]_n)$	(60)
$[Cdc14]_n = \max(0, [Cdc14_T]_n - \rho_{14,net1} \cdot [Net1_A]_n)$	(61)
$\frac{d[Polo_T]_n}{dt} = k_{s,polo,m1} \cdot [Mcm1_A]_n - (k_{d,polo} + k_{d,polo,h1} \cdot [Cdh1_A]_n) \cdot [Polo_T]_n$	(62)
$\frac{d[Polo_A]_n}{dt} = \gamma \cdot ([Polo_T]_n \cdot H(\sigma \cdot W_{polo}) - [Polo_A]_n)$	(63)
$W_{polo} = \omega_{a,polo,b2} \cdot [Clb2]_n - \omega_{i,polo}$	(64)
$\frac{d[Tem1_A]_n}{dt} = \gamma_{tem1} \cdot ([Tem1_T]_n \cdot H(\sigma \cdot W_{tem1}) - [Tem1_A]_n)$	(65)
$W_{tem1} = \omega_{a,tem1,lo} \cdot [Polo_A]_n - \omega_{i,tem1} - \omega_{i,tem1,px} \cdot [PPX_A]_n$	(66)
$\frac{d[Cdc15_A]_n}{dt} = \gamma \cdot ([Cdc15_T]_n \cdot H(\sigma \cdot W_{cdc15}) - [Cdc15_A]_n)$	(67)
$W_{cdc15} = \omega_{a,cdc15,14} \cdot [Cdc14]_n - \omega_{i,cdc15} - \omega_{i,cdc15,b2} \cdot [Clb2]_n$	(68)
$[Tem1_A : Cdc15_A]_n = \min([Tem1_A]_n, [Cdc15_A]_n)$	(69)
Definitions:	
$H(X) = 1/(1 + e^{-X})$; $Heav(x) = 1$, if $x \geq 0$, = otherwise	

Rules:

- 1) Bud emerges when $[BUD]_n = 1$.
- 2) DNA synthesis starts when $[ORI]_n = 1$; provided that $B_{oriflag} = 1$. Then $B_{oriflag}$ is reset to 0 and $B_{udna} = 1$.
- 3) Spindle assembly is complete and chromosomes are properly aligned when $[SPN]_n = 1$. Set $B_{spc} = 1$.
- 4) The cell divides asymmetrically between mother and daughter cells when $[Clb2]_n$ drops below K_{Ez} . The mother:daughter size ratio at birth, $(1-f):f$, is computed from the formula $f = 0.3364 \exp(22.2/T_d)$, where T_d = mass-doubling time of the culture [43]. In glucose medium ($T_d = 100$ min) the ratio is 58:42 and in galactose and raffinose media ($T_d = 150$ min) the ratio is 61:39. At cell division, $[BUD]_n$, $[SPN]_n$, B_{udna} and B_{spc} are all reset to 0.
- 5) $[ORI]_n$ is reset to 0 (origins of replication are relicensed) when $[Clb2]_n + [Clb5]_n$ drops below K_{Ez2} . Set $B_{oriflag} = 1$.

doi:10.1371/journal.pone.0153738.t004

transcription factor for Cln2 and Clb5 (Table 4, Eqs 24 and 31. We assume that the phosphorylation and dephosphorylation of Whi5 are independent of its binding to SBF (Table 4, Eq 25).

Functional SBF promotes the synthesis of Cln2 and Clb5. As Cln2 accumulates, it further phosphorylates Whi5, enabling faster production of Cln2 [55]. Cln3, Cln2, and Clb5 all promote bud emergence [56]. The BUD variable represents progression to bud emergence, and we assume that a bud emerges when $[BUD]_n = 1$ (Table 4, Eq 30).

Formulation of the S/G₂/M module. Fig 8B and Eqs 31–54 of Table 4 describe the S/G₂/M module. CKI (the collective name of Sic1 and Cdc6) is a stoichiometric inhibitor that keeps, as we assume, Clb5 and Clb2 inactive during G₁ phase. (In fact, Clb2 is inhibited by both Sic1 and Cdc6, whereas Clb5 is inhibited mainly by Sic1 and not by Cdc6 [47, 57, 58].) We track the total concentrations of Clb5, Clb2, and CKI by class-1 variables (Eqs 31, 32 and 33,

respectively) and use class-3 variables to calculate free forms of Clb5 and Clb2 (Eqs 36 and 37). In these equations, we assume that CKI has comparable association and dissociation rates with both Clb2 and Clb5, so that CKI is distributed equally between them. (Again, note that this is not true for Cdc6 [57].)

The rise of Cln2 after the START transition causes the phosphorylation and rapid degradation of CKI (Eqs 34 and 35) [59]. The falling level of CKI releases Clb5, which further phosphorylates CKI. Free Clb5 activates components responsible for DNA synthesis [60] (Eq 41). The ORI variable represents initiation of DNA replication, which starts (we assume) when $[\text{ORI}]_n = 1$.

Cln2 and Clb5 also inactivate Cdh1, a protein that degrades Clb2 during G₁ phase [61, 62] (Eqs 42 and 43), allowing Clb2 to accumulate. However, at this point (in late G₁-early S), the total concentration of Clb2 is low because its transcription factor, Mcm1, is inactive. Clb2 production ramps up as Clb2-dependent kinase activates its own transcription factor Mcm1 [53, 63] (Eqs 44 and 45). In addition, Clb2 phosphorylates and inactivates SBF [53, 54] (Eqs 27 and 28), thereby stopping synthesis of Cln2 and Clb5 and preparing the cell for mitotic exit.

Swi5 is the transcription factor for CKI [64] (Eq 33). We use a class-1 variable to track the total amount of Swi5 (Eq 38) and a class-2 variable to track its activity (Eq 39). Eq 39 calculates the activity of Swi5, $[\text{Swi5}_A]_n$, at steady state, assuming its phosphorylation and dephosphorylation are very rapid.

As the accumulation of Clb2 drives the cell into M phase, it also sets up conditions for mitotic exit by phosphorylating and activating the APC [65] (Eqs 46 and 47). APC activity—which requires the cooperation of an auxiliary subunit, Cdc20—is essential for chromosome segregation at the metaphase-anaphase transition [66, 67] and the initiation of mitotic cyclin degradation [68]. But, during early M phase, Cdc20 is kept inactive by the spindle assembly checkpoint (SAC) [69]. The SAC activates a checkpoint protein, Mad2, which sequesters and inactivates Cdc20. In our model, the Mad2-dependent checkpoint is invoked by the onset of DNA synthesis (when $[\text{ORI}]_n = 1$) and released once the mitotic spindle is fully assembled (when $[\text{SPN}]_n = 1$) (Eqs 48 and 49). The mitotic spindle starts to assemble, we assume, when the concentration of Clb2 exceeds a certain threshold (J_{spn}) and is complete when $[\text{SPN}]_n = 1$ (Eq 50). We use a class-1 variable to describe the total concentration of Cdc20 (Eq 51) and then compute the concentration of Cdc20_A (unbound to the active form of Mad2) using a class-3 variable (Eq 52).

Cdc20_A binds to both the phosphorylated and unphosphorylated forms of APC. Because Cdc20_A:APC is much less active than Cdc20_A:APC_P in degrading Clb5 and Clb2, the degradation of Clb proteins at the end of the cycle is dependent on both the phosphorylation of APC and the release of the spindle assembly checkpoint. Both processes are promoted by Clb2. We calculate the concentrations of Cdc20_A:APC_P and Cdc20_A:APC by Eqs 53 and 54, which are alternative forms of a class-3 variable. We assume tight binding between Cdc20_A and APC_P; so, the concentration of Cdc20_A:APC_P is the concentration of either Cdc20_A or APC_P, whichever is the lesser (Eq 53). Cdc20_A that is in excess of APC_P is assumed to bind tightly to APC (Eq 54). (We are assuming that Cdc20_A binds primarily to APC_P [65] and secondarily to unphosphorylated APC.)

Formulation of the Exit module. For a budding yeast cell to exit from mitosis and return to G₁ it must transiently activate a phosphatase, Cdc14, which dephosphorylates many proteins that had been phosphorylated by cyclin-dependent kinases in S/G₂/M. In particular, Cdc14 activates Cdh1 and CKI. These two factors stabilize G₁ phase of the cell cycle by repressing the activity of Clb-dependent kinases. The activation of Cdc14, as described by the EXIT module in Fig 8C, is accomplished by two pathways: FEAR (Cdc fourteen early anaphase release) and MEN (mitotic exit network) (for a review, see [70]). In the FEAR pathway, active Cdc20 cleaves Pds1 (securin) [66] and releases Esp1 (separase) [67]. Free Esp1 is responsible for chromatid

separation [67] and inactivation of PPX (PP2A^{Cdc55}), a phosphatase that dephosphorylates Net1 [71]. Subsequent phosphorylation of Net1 causes Cdc14 to be released from Net1:Cdc14 complexes in the nucleolus, and free Cdc14 is the phosphatase that drives exit from mitosis [71–75]. A schematic diagram of the FEAR pathway is: Cdc20 → Esp1—| PPX → Net1—| Cdc14.

We use a class-1 variable to describe the total concentration of Pds1 (Eq 55) and a class-3 variable to represent free Esp1, i.e., Esp1 that is not bound to Pds1 (Eq 56). The active forms of PPX and Net1 are described by class-2 variables (Eqs 57 and 59, respectively). The active (unphosphorylated) form of Net1 is a stoichiometric inhibitor of Cdc14, so we use a class-3 variable to represent free Cdc14 (Eq 61). In Eq 61 we introduce a stoichiometric factor, $\rho_{14,net1}$, in order to simulate two mutants, *net1-ts* and *TAB6-1*, that show reduced association between Net1 and Cdc14 [74–76]. For wild-type cells we set $\rho_{14,net1} = 1$ and for *net1-ts* and *TAB6-1* cells we set $\rho_{14,net1} < 1$.

The FEAR pathway is not sufficient to return cells to G₁ phase because Cdc14 activates Cdh1 which degrades Clb2, allowing Net1 to regain its ability to sequester Cdc14 in the nucleolus. To get robust phosphorylation of Net1 and full release of Cdc14 from the nucleolus, the FEAR pathway must be supplemented by the MEN pathway, whose role is to activate Cdc15 and Tem1 (see Fig 8C). Active Cdc15 then supports continued phosphorylation of Net1 even as Clb2-dependent kinase activity is dropping. Premature activation of Cdc15 is prevented by Clb2-dependent phosphorylation (inactivation) of Cdc15 in metaphase. Hence, Cdc15 activity is low as cells enter anaphase and rises abruptly as Clb2 is degraded by Cdc20_A:APC_P and Cdc14 is activated by the FEAR pathway (Eqs 67 and 68) [77].

Meanwhile, Polo kinase, which was activated in prometaphase when Clb2-kinase activity was high (Eqs 62–64) [78], is able to activate Tem1 after PPX is inactivated by the FEAR pathway (Eqs 65 and 66) [71, 79]. Together, Tem1 and Cdc15 form an active complex (Tem1_A:Cdc15_A) (Eq 69) that phosphorylates Dbf2/Mob1 (not modeled explicitly), which then phosphorylates and inactivates Net1, resulting in full Cdc14 release. In this way, the transient release of Cdc14 by the FEAR pathway initiates a positive feedback loop between the activation of Tem1_A:Cdc15_A (MEN) and further release of Cdc14 [42].

Full release of Cdc14 re-sets the cell to G₁ by two complementary actions. First of all, Cdc14 dephosphorylates and activates Cdh1, and active Cdh1 (in association with APC) fully degrades Clb2 [68, 80, 81] and Polo kinase [82]. In addition, Cdc14 stabilizes CKI and activates its transcription factor, Swi5 [62, 83]. Abundant CKI and active Cdh1 are characteristic molecular signatures of G₁ phase in budding yeast.

We assume that cell division occurs when the concentration of Clb2 drops below a threshold value, K_{EZ} . Because budding yeast cells divide asymmetrically, we set the sizes of mother and daughter cells after division equal to 58% and 42% of the size of the dividing cell in glucose medium, which are close to the proportions observed by Di Talia *et al.* [36]. In galactose medium, for which cells grow more slowly and divide more asymmetrically [84], we take these proportions to be 61% and 39%.

BUD, ORI, and SPN, the dimensionless variables used to mark bud emergence, onset of DNA synthesis, and spindle assembly, are reset to 0 as the cell exits mitosis. We reset [BUD]_n and [SPN]_n to 0 at cell division, when [Clb2]_n = K_{EZ} . We reset [ORI]_n to 0 when [Clb2]_n+ [Clb5]_n drops below K_{EZ2} , because origins of replication are relicensed only if all Clb-dependent kinase activity is extinguished in G₁ phase.

Full lists of initial conditions and kinetic constants used to simulate wild-type cells are given in Tables 3 and 5, respectively.

The full SCM (Table 4) tracks 33 protein species (not counting V, BUD, ORI and SPN) and requires ~100 parameter settings (Table 5). By comparison, Chen-2004 tracks the same number of protein species and requires ~120 parameter settings.

Table 5. Parameter values for wild-type cells.

Rate constants (min ⁻¹) (subscripts: “s” for synthesis, “d” for degradation)							
$k_{s,bck2}$	0.00675	$k_{d,bck2}$	0.5				
$k_{s,bud,e}$	0.33	$k_{d,bud}$	0.01				
$k_{s,cdc20}$	0.006	$k_{s,cdc20,m1}$	0.6	$k_{d,cdc20}$	0.3		
$k_{s,cki}$	0.024	$k_{s,cki,swi5}$	0.24	$k_{d,cki}$	0.005	$k_{d,ckip}$	1.7
$k_{s,clb2}$	0.0066	$k_{s,clb2,m1}$	0.044				
$k_{d,clb2}$	0.003	$k_{d,clb2,20}$	0.14	$k_{d,clb2,20,i}$	0.0366	$k_{d,clb2,h1}$	0.6
$k_{s,clb5}$	0.0006	$k_{s,clb5,bf}$	0.029				
$k_{d,clb5}$	0.012	$k_{d,clb5,20}$	0.1	$k_{d,clb5,20,i}$	0.015		
$k_{s,cln2}$	0	$k_{s,cln2,bf}$	0.27	$k_{d,cln2}$	0.12		
$k_{s,cln3}$	0.11	$k_{d,cln3}$	0.4				
$k_{s,ori,e}$	2	$k_{d,ori}$	0.06				
$k_{s,pds1}$	0.03	$k_{d,pds1}$	0.05	$k_{d,pds1,20}$	3	$k_{d,pds1,20,i}$	0.3
$k_{s,polo,m1}$	0.03	$k_{d,polo}$	0.01	$k_{d,polo,h1}$	0.1		
$k_{s,swi5}$	0.005	$k_{s,swi5,m1}$	0.08	$k_{d,swi5}$	0.08		
$k_{s,spn}$	0.1	$k_{d,spn}$	0.06				
Other time-scale factors (min ⁻¹)							
μ	0.00693	(mcd = 100 min in glucose medium)					
γ	1	γ_{cki}	2	γ_{apc}	0.8	γ_{tem1}	0.1
Interaction coefficients (dimensionless) (subscripts: “a” for activation, “i” for inactivation, “p” for phosphorylation, “dp” for dephosphorylation)							
$\omega_{a,apc,b2}$	0.65	$\omega_{i,apc}$	1				
$\omega_{a,cdc15,14}$	15	$\omega_{i,cdc15}$	1	$\omega_{i,cdc15,b2}$	0.25		
$\omega_{a,cdh1}$	1	$\omega_{a,cdh1,14}$	4.3	$\omega_{i,cdh1,e}$	1	$\omega_{i,cdh1,n3}$	1
$\omega_{i,cdh1,n2}$	0.6222	$\omega_{i,cdh1,b5}$	4.5	$\omega_{i,cdh1,b2}$	2.8		
$\omega_{p,cki,n3}$	4.2	$\omega_{p,cki,k2}$	0.4	$\omega_{p,cki,n2}$	0.3556	$\omega_{p,cki,b5}$	1.5
$\omega_{p,cki,b2}$	2.2	$\omega_{dp,cki}$	1	$\omega_{dp,cki,14}$	1.8		
$\omega_{a,mad2}$	20	$\omega_{i,mad2}$	0.4				
$\omega_{a,mcm1,b2}$	5	$\omega_{i,mcm1}$	3				
$\omega_{p,net1,b2}$	0.125	$\omega_{p,net1,en}$	1	$\omega_{p,net1,15}$	0.03		
$\omega_{dp,net1}$	0.1	$\omega_{dp,net1,14}$	0.1	$\omega_{dp,net1,px}$	3		
$\omega_{a,polo,b2}$	5	$\omega_{i,polo}$	1				
$\omega_{a,ppx}$	1	$\omega_{i,ppx,pl}$	3				
$\omega_{p,sbf,b2}$	2.5	$\omega_{dp,sbf}$	1				
$\omega_{a,swi5,14}$	2	$\omega_{i,whi5,b2}$	4.25				
$\omega_{a,tem1,lo}$	6	$\omega_{i,tem1}$	1	$\omega_{i,tem1,px}$	22		
$\omega_{p,whi5,n2}$	1.7778	$\omega_{p,whi5,n3}$	12	$\omega_{p,whi5,k2}$	16	$\omega_{p,whi5,b5}$	0
$\omega_{dp,whi5}$	1	$\omega_{dp,whi5,14}$	0.5				
Total concentrations (dimensionless)							
$[APC_T]_n$	25	$[Cdc14_T]_n$	2	$[Cdc15_T]_n$	1	$[Cdh1_T]_n$	1
$[Esp1_T]_n$	0.5	$[Mcm1_T]_n$	1	$[Net1_T]_n$	3.55	$[PPX_T]_n$	1
$[SBF_T]_n$	1	$[Tem1_T]_n$	2	$[Whi5_T]_n$	2.5	$[Mad2_T]_n$	25
Other parameters (dimensionless)							
D_{cln3}	1	$e_{bud,b5}$	0.25	$e_{bud,n2}$	0.4444	$e_{bud,n3}$	0.2
$e_{ori,b2}$	0.35	$e_{ori,b5}$	0.21	J_{cln3}	6	J_{spn}	0.26
K_{EZ}	0.4	K_{EZ2}	0.4	$\rho_{14,net1}$	1		
σ	10	σ_{net1}	8				
Extra parameters used in stochastic simulations							
K_{flag}	0.8						
k_{tr}	0.15 protein molecules per mRNA molecule per fL per min for all proteins						

(Continued)

Table 5. (Continued)

k_{dm}	0.7 min ⁻¹ for all mRNAs
$\langle m_{min} \rangle$	5 mRNA molecules for <i>CLN2</i> , <i>CKI</i> , <i>CLB5</i> , <i>CLB2</i> , and <i>PDS1</i> , and 0 mRNA molecule for all other genes

doi:10.1371/journal.pone.0153738.t005

8. Deterministic simulations of wild-type and mutant cells

To simulate cell cycle progression in wild-type and mutant yeast cells, we solve the ODEs in [Table 4](#) with the parameter values in [Table 5](#). To simulate a broad selection of mutant yeast strains ([S3 Table](#)), we made appropriate changes to the “wild-type” parameter values, as outlined in [S4 Table](#).

Our choice of wild-type parameter values ([Table 5](#)) was guided initially by the rate constant assignments in Chen *et al.* [41] and then adjusted manually to give a good fit to the observed phenotypes of the 133 mutant strains in [S3 Table](#). We were able to account for the observed phenotypes of 125 of the 133 mutant strains (94%) in the data set we used to constrain the model. We tried automatic exploration of parameter space by a genetic algorithm (“Differential Evolution”) but could not find a set of parameter values that improves on the 94% success rate achieved manually [85].

The simulation of wild-type cells ([Fig 9](#)) shows oscillating patterns of cell cycle control variables that are in agreement with observations and expectations. The *START* transition ([Fig 9A](#)) is initiated by the inactivation of *Whi5* as *Cln3* accumulates, followed by the positive feedback-driven expression of *Cln2*. [Fig 9B](#) shows an alternating pattern of *G*₁ phase (during which *G*₁ stabilizers *CKI* and *Cdh1* are abundant) and *S/G*₂/*M* phase (during which *Clb5* and *Clb2* are abundant). During mitotic exit, the release of *Cdc14* resets the system back to *G*₁ phase. Quantitative comparisons to experimental data will be discussed in the next section on stochastic simulations.

To verify our model, we computed the expected phenotypes of 133 mutant strains ([S3 Table](#)) and compared our results to the original model of Chen *et al.* [41] and to available experimental observations. (See our web site at <http://mpf.biol.vt.edu> for the observed phenotypes of mutant strains and references to the original literature.) Simulations that exhibit periodic cell division correspond to viable mutants, and simulations that arrest at some point in the cell cycle correspond to inviable mutants, with phenotypes assigned according to the rules in [S5 Table](#). In our simulations, 125 mutants show phenotypic characteristics in agreement with the original model and experiments. (Notice that our SCM achieves the same accuracy as Chen-2004.) The eight mutant simulations that are not in agreement with observed phenotypes are listed in [S6 Table](#) and discussed in detail in [S5 Text](#).

9. A stochastic SCM of the budding yeast cell cycle

In this section, we construct a stochastic version of our SCM, in order to address three questions. (1) Is our model of the cell cycle control system robust in the face of inevitable molecular fluctuations within single cells? (2) Is a stochastic version of our model consistent with quantitative measurements of cell cycle variability among wild-type cells? (3) Do stochastic models behave differently than deterministic models under some circumstances? With regard to the third question, we have in mind situations where mutations may make the regulatory mechanism less robust and more sensitive to molecular noise. For example, in the double mutant strain *CLB2-dbΔ clb5Δ* (*CLB2* destruction box deletion and *CLB5* gene deletion) some cells are able to complete the cell cycle and divide whereas other cells become arrested in telophase and eventually die, as originally observed by Cross [86] and confirmed by Ball *et al.* [87]. This sort

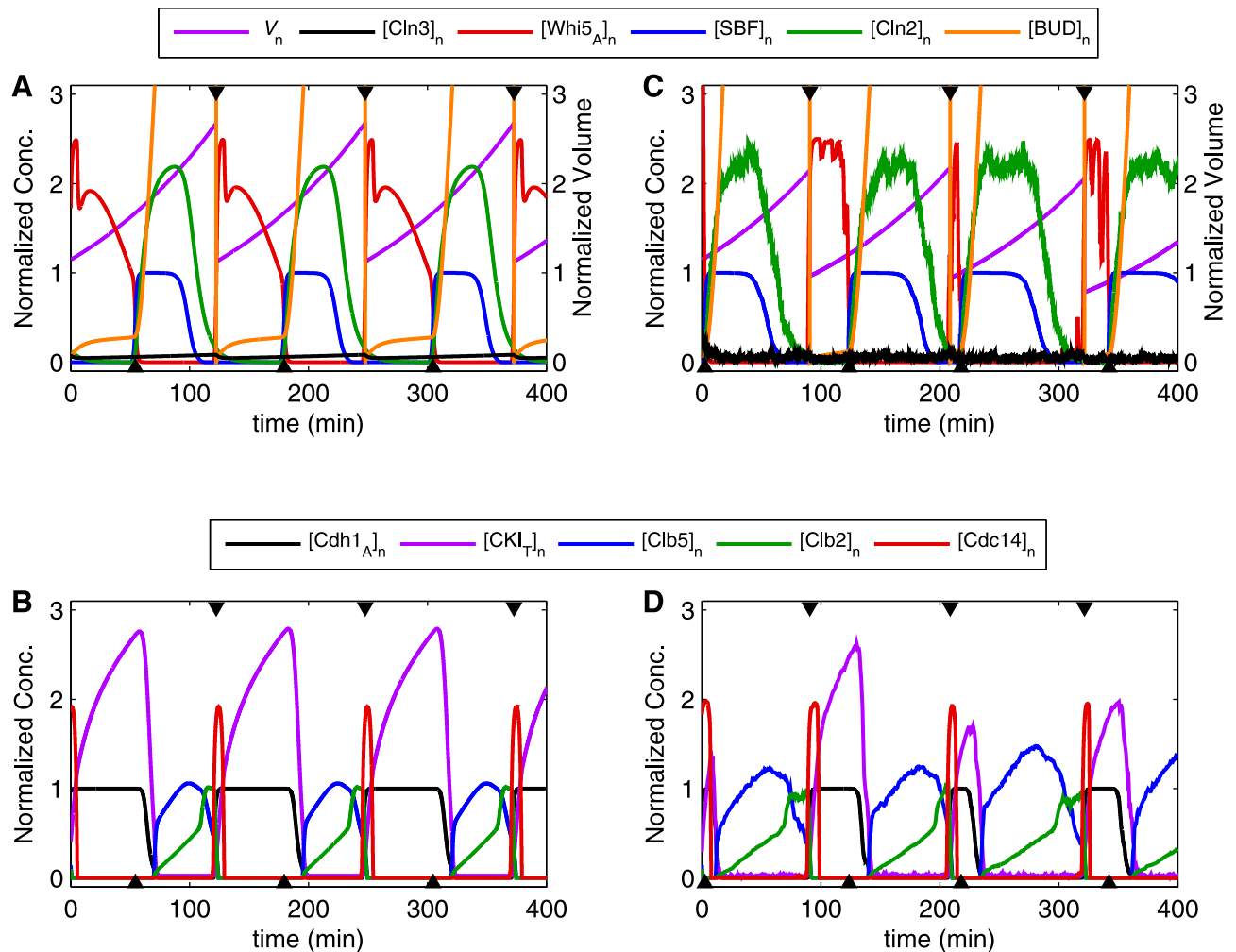


Fig 9. Simulations of wild-type cells. (A) *START*: As the cell grows (increasing V_n), Cln3 accumulates and phosphorylates Whi5. At a critical cell size, SBF is abruptly released from the inactive SBF:Whi5 complex and initiates a positive feedback loop between the accumulation of Cln2 and the phosphorylation of Whi5. (B) *G₁/S/G₂/M*: SBF also promotes the synthesis of Clb5. Once Clb5 titrates out CKI, then Clb5 and Cln2 together inactivate Cdh1, resulting in the accumulation of Clb2. *EXIT*: Clb2 triggers many mitotic events, eventually leading to the release of Cdc14 during mitotic exit. When Clb2 drops below a normalized concentration of 0.4, the cell divides asymmetrically between daughter and mother cells. The daughter cell receives 42% of the cell size at division, and the mother cell (not shown here) receives the remaining 58%. (C and D) The stochastic model shows the typical fluctuations of protein concentrations around the average dynamics predicted by the corresponding deterministic model. For easier comparison to the deterministic simulation (A and B), we converted the numbers of molecules reported by the stochastic simulation to normalized concentrations. *START* and division events are indicated by up-pointing and down-pointing black triangles, respectively.

doi:10.1371/journal.pone.0153738.g009

of partial viability is clearly incompatible with a deterministic model of the cell division cycle but may be accommodated by a stochastic model.

With regard to question (2), single-cell experimental techniques (e.g., flow cytometry and live-cell imaging of fluorescent proteins) have revealed much information about cell-to-cell variation among genetically identical cells. In budding yeast, fluorescence microscopy has been used to study proteins that regulate cell cycle progression and to determine the onset of cell cycle events such as Start, bud emergence, and cell division in individual cells [38, 88, 89]. In addition, fluorescence in situ hybridization (FISH) has been used recently to quantify mRNA levels in individual yeast cells [90], determining that a yeast cell carries roughly 5–15 mRNA molecules of each gene measured, including a sample of cell cycle control genes [91]. Since the

number of mRNA molecules directly determines the production rate of its protein product, noise due to low, fluctuating numbers of mRNA molecules will be significantly amplified as fluctuations in protein abundance [39]. Consistent with this expectation, stochastic simulations by Kar et al. [92] suggested that mRNA noise is a major source of fluctuations in the budding yeast cell cycle control system. Therefore, to understand stochasticity in the system, inclusion of mRNA noise seems to be necessary. The stochastic version of SCM described above was designed specifically to deal with molecular noise derived from both protein and mRNA fluctuations.

Model conversion. In our deterministic model (Eqs 21–69) that we reformulated from Chen-2004, the variables ($[Cln2]_n$, $[Clb2]_n$, etc.) represent concentrations in “normalized” units (i.e., scaled with respect to a characteristic concentration of each component). Stochastic studies, on the other hand, measure protein abundances in terms of numbers of molecules. Before constructing the stochastic model, we first convert the normalized concentration units used in the deterministic SCM into numbers of molecules using the conversion process described in [93]. The details of the model conversion are discussed in S6 Text.

The stochastic model. After converting “normalized concentrations” to “numbers of molecules” we add molecular noise to class-1 variables by the Langevin formalism, as described above. For example, the stochastic rate equation for the total number of Clb5 molecules is:

$$\begin{aligned} \frac{dClb5_T}{dt} = & A_{clb5} - B_{clb5} \cdot Clb5_T \\ & + \sqrt{A_{clb5} + B_{clb5} \cdot Clb5_T} \cdot \frac{\zeta_1(t)}{\sqrt{\Delta t}} \\ & + Clb5_T \sqrt{2B_{clb5} \frac{k_{tr} \cdot V_{fl}}{A_{clb5} + \langle m_{min} \rangle \cdot k_{tr} \cdot V_{fl}} \cdot \frac{B_{clb5}}{B_{clb5} + k_{dm}}} \cdot \frac{\zeta_2(t)}{\sqrt{\Delta t}}, \end{aligned} \quad (70)$$

$$\text{where } A_{clb5} = \varphi \cdot c_{clb5} \cdot k_{s,clb5} + \frac{c_{clb5}}{c_{sbf}} \cdot k_{s,clb5,bf} \cdot SBF + \mu \cdot Clb5_T$$

$$\text{and } B_{clb5} = k_{d,clb5} + \frac{k_{d,clb5,20}}{\varphi \cdot c_{cdc20}} \cdot Cdc20_A : APC_p + \frac{k_{d,clb5,20,i}}{\varphi \cdot c_{cdc20}} \cdot Cdc20_A : APC,$$

where A_{clb5} and B_{clb5} are the converted versions of the synthesis and degradation rates from the deterministic model (see S6 Text for details). The mRNA-inherited noise term in Eq 70 is slightly different from the term in Eq 19 because our full model does not account explicitly for the mRNA species (see S7 Text for the derivation of Eq 70). k_{tr} is the protein translation rate (the number of protein molecules produced per mRNA molecule per fL per min). $V_{fl} = V_n \cdot c_{vol}$ is cell volume in fL, where c_{vol} is average cell size at birth of wild-type daughter cells (28 fL). $\langle m_{min} \rangle$ is the minimum number of mRNA molecules of each gene always present in the cell. k_{dm} is the mRNA degradation rate. We treat k_{tr} , $\langle m_{min} \rangle$, and k_{dm} as tuning parameters. (See S8 Text for the discussion of the choices of $\langle m_{min,i} \rangle$ in our model.) $\zeta_1(t)$ and $\zeta_2(t)$ are independent random variables chosen from a normal distribution $N(0, 1)$ with mean = 0 and standard deviation = 1. A term, $\mu \cdot Clb5_T$, is added the production rate to make for consistency between the deterministic and stochastic models (see discussion in S6 Text). c_{clb5} , c_{sbf} and c_{cdc20} are the characteristic concentrations (in nmol/L) for the indicated proteins (listed in Table 3), and $c_s \cdot V_{fl} \cdot N_A \cdot 10^{-9} \cdot 10^{-15} = c_s \cdot \varphi$ is the characteristic number of molecules of species S in volume V_{fl} , where $\varphi = 0.6 V_{fl}$.

In our deterministic model, the cell divides whenever the normalized concentration of Clb2 drops below a threshold K_{EZ} . In the stochastic model, fluctuations around the threshold could cause multiple division events. To avoid this problem, we add an extra condition to the rule for

cell division in the stochastic model: (1) a cell divides when $[\text{Clb2}]_n$ drops below the threshold K_{EZ} , and (2) the cell cannot divide again until $[\text{Clb2}]_n$ increases above a higher threshold K_{flag} ($K_{\text{flag}} > K_{EZ}$).

We do not add molecular noise to variables of classes 2 and 3, because we assume they change on much faster time scales than class-1 variables and therefore regress quickly to their mean values.

In addition to molecular noise from protein and mRNA fluctuations, budding yeast cells are also subject to variations in the cell division process itself. In our simulations, the daughter cell receives, on average, 42% of the volume and constituent proteins of the dividing cell, with a standard deviation of 5%.

The values of the extra parameters used in our stochastic simulations are listed in [Table 5](#).

10. Stochastic simulations of wild-type and mutant cells

Stochastic simulations of wild-type cells (e.g., [Fig 9C and 9D](#)) show high variability in progression through the cell cycle. Following the lead of Cross and his group [38], we divide the cell cycle into three periods: T_1 , T_2 , and T_b . T_1 is the duration from cell birth to START , which we identify with SBF reaching 50% of its maximum value. T_2 is the period from START to bud emergence, which we identify with $[\text{BUD}]_n = 1$. Finally, T_b is the duration of the “budded phase,” from bud emergence to the next cell division.

From stochastic simulations of wild-type cells, we computed means and variances of T_1 , T_2 , T_b , cell cycle duration, and cell size at birth, which we compare to experimental observations [38] in [Fig 10](#). (The full distributions of T_1 , cell cycle duration and V_{birth} , for both mother and daughter cells, are shown in [S7 Fig](#).) Overall, our results show a reasonable agreement with the experimental data, although there are some quantitative discrepancies. Our simulated T_1 is longer and our simulated T_2 is shorter than observed in both mother and daughter cells, which may be attributed to a difference between our theoretical criterion for START (SBF reaching 50% of its maximum activity) and the experimental criterion for START (Whi5 disappearance from the nucleus). $T_1 + T_2 = T_{G1}$ = duration of the “unbudded phase” is longer than observed in mother cells, but quite accurate for daughter cells. The predicted and observed CVs of T_{G1} are all ~50%. In our simulations the average delay from bud emergence (when $[\text{BUD}]_n = 1$) to the initiation of DNA synthesis (when $[\text{ORI}]_n = 1$) is ~12 min, which is inconsistent with the observation that the two events occur nearly simultaneously in wild-type cells.

Fluctuations in both mRNA and protein are needed to account for the variability observed in wild-type cells. In [Fig 10](#), we decompose the effects of noise in our model by comparing four different cases: the full stochastic SCM, the stochastic SCM without the mRNA-inherited noise term in [Eq 70](#), the deterministic SCM with “extrinsic” noise only (retain 5% variation in the cell division process, which is one component of extrinsic noise, but no intrinsic noise terms in [Eq 70](#)), and the completely deterministic SCM. (The full distributions for the first three cases are presented in [S7 Fig](#).) The full stochastic model with protein and mRNA fluctuations clearly shows the highest variations, which are comparable to the experimental values. Interestingly, noise contributes significantly to the behavior of wild-type daughter cells before START , because the full stochastic simulation predicts an average T_1 duration (27 min) that is markedly shorter than the result from the model without mRNA fluctuations (44 min), the extrinsic-only model (58 min), and the deterministic model ($T_1 = 59$ min, no variability). In our model, the major source of intrinsic noise comes from fluctuations of Cln3 and Bck2, because the average total amount of Cln3 is quite small (~100 molecules) [31] and we assume that Bck2 has a similar abundance. Since the START transition is driven by a bistable switch [36], high fluctuations of Cln3 and Bck2 combined with the positive feedback loop

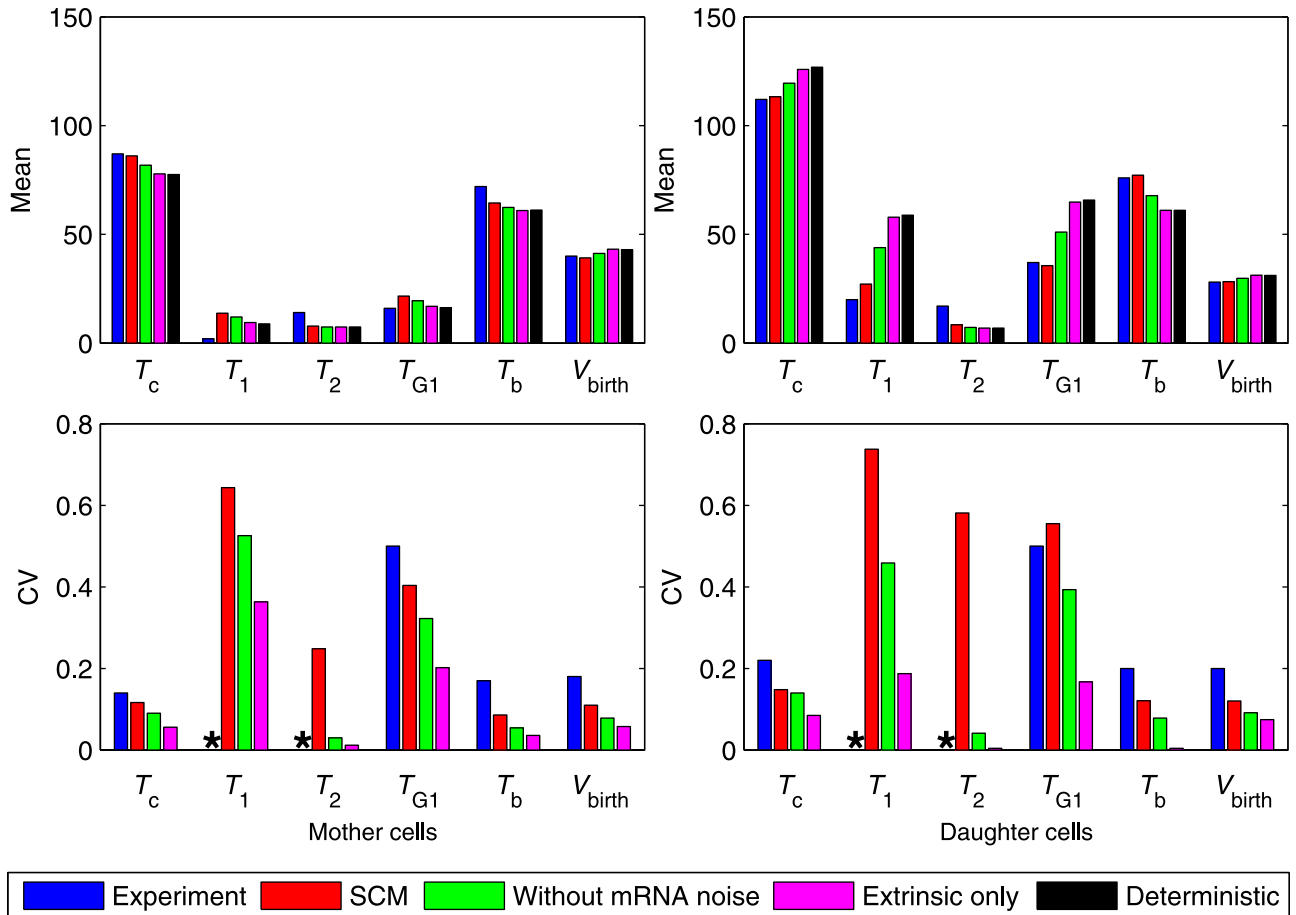


Fig 10. Statistical properties of cell cycle progression. Experimental observations for wild-type cells [38] (blue bars) are compared to simulations from four different cases of our model: the full stochastic SCM (red bars), the stochastic SCM without the mRNA-inherited noise term (green bars), the deterministic SCM with “extrinsic” noise only (magenta bars), and the completely deterministic SCM (black bars). T_c is cell cycle duration (min) = $T_{G1} + T_b = T_1 + T_2 + T_b$. T_1 is the duration from cell birth to START (min), which we identify with SBF reaching 50% of its maximum value. T_2 is the period from START to bud emergence (min), which we identify with $[BUD]_n = 1$. $T_{G1} = T_1 + T_2 =$ duration of the “unbudded phase” (min). T_b is the duration of the “budded phase,” from bud emergence to the next cell division (min). V_{birth} is cell size at birth (fL). Asterisks indicate unreported data.

doi:10.1371/journal.pone.0153738.g010

engaged by Cln2 can result in T_1 duration that is much shorter than what is predicted by the deterministic system. This shortening of T_1 is a genuine divergence of the stochastic model from the deterministic model. In the deterministic model, the cell cannot execute START until it surpasses the saddle-node bifurcation point (Fig 2) where the pre-START steady state disappears. In the stochastic model, however, molecular fluctuations can induce premature transitions from the “excitable” pre-START steady state to the much more stable post-START steady state before the system reaches the saddle-node bifurcation point [94].

The duration of G_1 is negatively correlated with birth size in experiment and in simulation. Next, we study the correlation between size at birth and duration of G_1 phase (T_{G1}). If cell cycle progression during G_1 is perfectly controlled by cell size, then a plot of μT_{G1} against $\ln(V_{birth})$ should give a straight line with slope = -1 [38], where μ is the specific growth rate and V_{birth} is the birth size of cells. In the experiment of Di Talia *et al.* [38], small daughter cells show the expected negative correlation (slope = -0.7), indicating a strong size-control mechanism operating in small budding yeast cells. Larger daughter cells show less negative

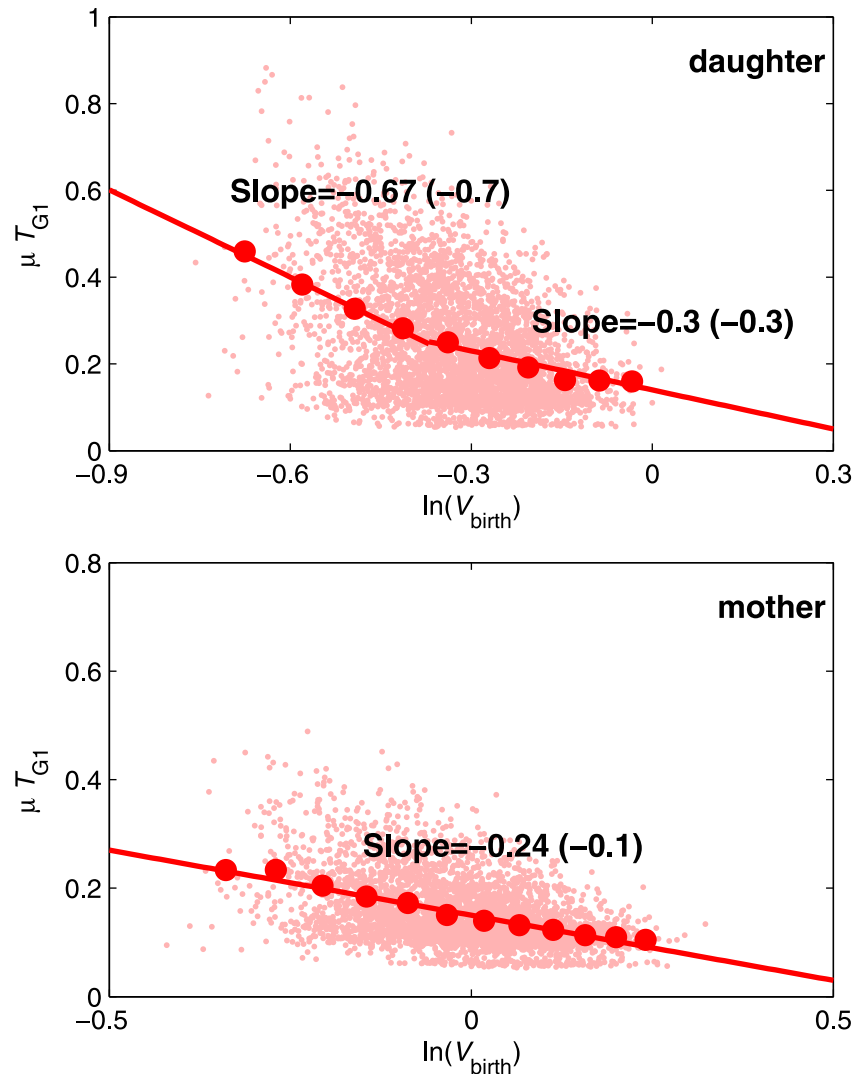


Fig 11. The joint distributions of cell size at birth and G_1 phase duration predicted by our stochastic model of the full cell cycle control system. (Upper panel) Daughter cells. (Lower panel) Mother cells. T_{G1} is the duration from cell birth to bud emergence, and μ is the specific growth rate of the cell culture. In the plots, cell size is normalized by the average size of mother cells at birth and is plotted on a log scale. Small dots in the background represent data collected from simulations of individual cells. Large dots represent average $\mu \cdot T_{G1}$ of the small dots binned in 2 fL intervals. For daughter cells, the binned data can be divided into two groups (small and large cells; break point at $\ln(V_{birth}) = -0.37$) and fitted by two straight lines with slopes of -0.67 and -0.30 (respectively). Mother cells can be fitted by one straight line with slope -0.24 . The experimental slope values, as reported by Di Talia *et al.* [38], are shown in parentheses. The binned data for mother cells is slightly better fit by two straight lines with a break point at $\ln(V_{birth}) = 0$.

doi:10.1371/journal.pone.0153738.g011

correlation (slope = -0.3). Mother cells seem to operate with little or no size control (slope = -0.1). In good accord with experimental observations, our simulations (Fig 11) show that the small and large daughter cells exhibit correlations with slopes -0.67 and -0.30 , respectively. The break between strong size control and weak size control occurs at a birth size of $\sim 0.69 \times \bar{V}_m$, where \bar{V}_m = average size of mother cell at birth. The mother cells show less correlation (slope = -0.24).

It is beyond the scope of this paper to provide a statistically rigorous analysis of the negative correlation between G_1 duration and size at birth predicted by the SCM. In a separate study, we

have fitted our simulations to the full experimental distributions (kindly provided by Stefano Di Talia). We subdivided the empirical joint distribution into 17 rectangles (“bins”) so that no bin contained more than about 20 cells or less than 3, and we subdivided the simulated joint distribution in an identical fashion. Then we computed the Hellinger distance between the two distributions (empirical and simulated) and minimized the distance by a quasi-Newton algorithm for stochastic optimization [95]. By using the full distribution (rather than the two-slope representation) we were able to improve the fit of the model to the data, but there remained a noticeable discrepancy in that the model predicts longer tails of G_1 durations than are observed experimentally for both mother and daughter cells. Hence, although the model is qualitatively in accord with the observed negative correlation between T_{G1} and birth size, it exhibits long tails in the T_{G1} distributions that appear to be statistically significant deviations from observed G_1 durations. These results will be reported in full in a later publication.

In [S8 Fig](#) we plot the correlations of cell size at birth with both T_{G1} and T_1 and confirm the experimental observation [38] that $T_2 = T_{G1} - T_1$ is relatively constant. This observation indicates that the size control mechanism in budding yeast operates at the *START* transition, i.e., at the phosphorylation and inactivation of Whi5. Whi5 inactivation frees up SBF to drive Cln2 and Clb5 production. The initial phosphorylation of Whi5 is the job of Cln3 and Bck2, and since their rates of accumulation are proportional to cell size, V , small cells take a longer time to inactivate Whi5, and large cells take a shorter time.

Simulated numbers of protein molecules for an asynchronous population are in agreement with observations. Next, we study the abundances of protein species in an asynchronous population, as might be measured experimentally. To this end, for each simulated cell we select a random time point between birth and division and record the number of each protein species present at that time. To obtain a sample of time points representative of an asynchronous population of cells, we must take into account that the number of newborn cells is twice the number of dividing cells. Hence, we select a random number θ , $0 \leq \theta \leq 1$, from an exponential probability density function

$$f(\theta) = \ln(2) \cdot 2^{1-\theta} \tag{71}$$

and then calculate $t_{\text{birth}} + (t_{\text{division}} - t_{\text{birth}}) \cdot \theta$ as a random time point in each complete cell division cycle. By this prescription, the probability of choosing a cell at birth is twice the probability of choosing a cell at division. ([Eq 71](#) is not exactly correct for asymmetrically dividing cells, like budding yeast, but the errors introduced by this approximation are minor.)

This set of simulated protein abundances should be comparable to numerical values collected from an asynchronous population of yeast cells. In [Table 6](#) we show that our computed average protein abundances are in good agreement with experimental values [31, 96], except for Clb5 and Clb2, whose predicted abundances are two-fold larger and smaller, respectively, than observed.

Stochastic simulations of the mutant strain *CLB2-dbΔ clb5Δ* explain its partial viability when growing on raffinose medium. Next we study viability of the mutant strain *CLB2-dbΔ clb5Δ*. In this strain, Clb2’s destruction box has been deleted from the *CLB2* gene, so Clb2 protein cannot be degraded by Cdc20 and only partially so by Cdh1 [86]. This mutant strain is inviable on glucose medium (mass-doubling time = $mdt = 100$ min) but can be partially rescued on raffinose medium, which supports slower growth ($mdt = 150$ min) [86, 87]. Obviously, “partial viability” (some cells complete the cell cycle and some do not) cannot be explained by a deterministic model in which all cells behave the same. A stochastic version of Chen’s 2004 model [87] predicts that some mutant cells, growing in raffinose, divide properly while others fail to exit from mitosis. However, the model in [87] applied Gillespie’s SSA directly to Chen’s

Table 6. Average protein abundances.

Protein name	Simulation (per haploid cell)	Experiment [96] (per haploid cell)	Experiment [31] (per diploid cell)
Cdc15	249	238	-
CKI (Sic1+Cdc6)	626	768*	214*
Clb1+Clb2	382	693	1,625
Clb5+Clb6	982	-	876
Cln1+Cln2	1,511	1,589	3,006
Cln3	83	-	216
Net1	1,991	1,590	-
PPX	3,116	3,170	-
Tem1	499	573	-
Whi5	1,714	1,440	-

*only Sic1 data is available.

doi:10.1371/journal.pone.0153738.t006

2004 model without unpacking the complex rate laws into elementary steps, and it did not take into account transcription-translation coupling. Hence, the results of the model in [87], though suggestive, are not very reliable. It is challenging to test whether our SCM approach provides a better account of the properties of this mutant strain.

Since the mutant cells cannot survive on glucose medium and are only partially viable on raffinose, the mutant strain is kept viable in the laboratory by introducing the *GAL-SIC1* gene into the *CLB2-dbΔ clb5Δ* cells and growing the strain in galactose, where Sic1 is overexpressed. In Fig 12, top panel, we show predicted growth curves for *CLB2-dbΔ clb5Δ GAL-SIC1* cells grown in media containing galactose (*GAL-SIC1* is “on”) or raffinose (*GAL-SIC1* is “off”). These cells proliferate in galactose with a population number-doubling time (*ndt*) ≈ 150 min, which is equal to the mass-doubling time (*mdt*) of individual cells. On the other hand, for the triple mutant cells growing in raffinose, *ndt* > 150 min, indicating that some cells are inviable. Cell viability is better illustrated in Fig 12, bottom panel, where we plot cumulative distribution functions for triple-mutant cells in galactose and in raffinose. Greater than 90% of the cells growing in galactose (*mdt* = 150 min and Sic1 overexpressed) complete the cell cycle within 250 min of birth, indicating that they are mostly viable. On the other hand, for the same cells growing in raffinose (*mdt* = 150 min but Sic1 not overexpressed), ~ 25% of the cells are undivided even 300 min after birth, indicating that ~25% of the cells growing in raffinose never complete the cell division cycle. This result agrees well with the experimental observation [87] that ~15–40% of these mutant cells never divide in raffinose growth medium. Furthermore, our simulations of mutant cells grown in glucose medium (*mdt* = 100 min and Sic1 not overexpressed) show less than 10% viability, which is consistent with the fact that these cells are inviable in glucose medium [86]. In Table 7, we compare the statistical properties of this mutant strain grown in raffinose from simulations and from experimental measurements [87].

As in the original model of Chen *et al.* [41], we assume that the synthesis of Clb2 is dependent on cell size. By this assumption, cell size at the onset of mitotic exit is critical for the cell's fate. Cells with larger size at the onset of mitotic exit have more Clb2 and are less likely to exit from mitosis. (Cells exit only if Clb2 is degraded below a threshold concentration.) In wild-type cells, the presence of both Cdc20 and Cdh1 ensures that Clb2 is fully degraded during mitotic exit. However, Clb2 protein encoded by the *CLB2-dbΔ* gene lacks the sequence targeted by Cdc20 and can be only partially degraded by Cdh1. To exit from mitosis, *CLB2-dbΔ* cells depend critically on the activation of Cdh1 and Sic1, but both Cdh1 and Sic1 are also inhibited

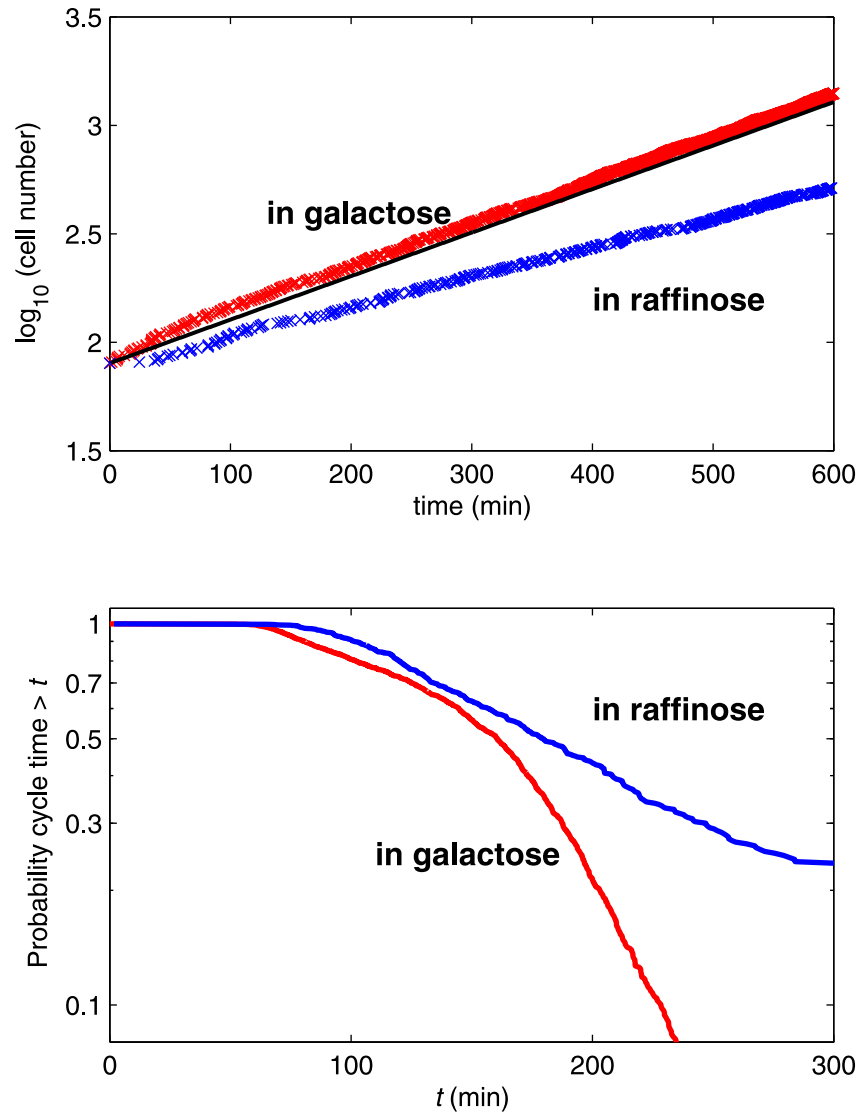


Fig 12. Growth curves and cycle time distributions for *CLB2-dbΔ clb5Δ GAL-SIC1* cells. (Upper panel) Logarithm of the total number of cells is plotted against time. The increase in cell number for *CLB2-dbΔ clb5Δ GAL-SIC1* cells growing in galactose (red crosses; Sic1 overexpressed) indicates exponential growth (black line) with the number doubling time = 150 min. The number doubling time of the same cells growing in raffinose (blue crosses; normal level of Sic1) is greater than 150 min, indicating that some cells do not complete the cell cycle when *GAL-SIC1* is not expressed. (In our simulations, the mutant cells are assumed to have mass doubling time = 150 min in both galactose and raffinose media.) (Lower panel) Cumulative distributions of cycle times for *CLB2-dbΔ clb5Δ GAL-SIC1* cells growing in galactose medium (red line) or in raffinose medium (blue line). The ordinate, $P(t)$, is the probability that a simulated cell has a cycle time greater than t .

doi:10.1371/journal.pone.0153738.g012

by Clb2-dependent kinase. When grown on a rich medium such as glucose, the mutant strain has a high growth rate and Clb2 accumulates to such a high level that it keeps Cdh1 and Sic1 inactive, resulting in telophase arrest. On a slower growth medium such as raffinose or galactose, a cell may exit from mitosis if Cdh1 and Sic1 can suppress Clb2. This explains why cells show high viability when Sic1 is overexpressed in galactose. In raffinose, however, without the help of Sic1 overexpression, noise plays a major role in determining whether or not a cell can

Table 7. Statistical properties of simulated *CLB2-dbΔ clb5Δ* cells in raffinose. Mean cycle time (in minutes) with standard deviation in parentheses.

	Our Simulation	Experiments [87]*			Simulation in [87]
		1	2	3	
Mother cells	150 (50)	151 (65)	165 (63)	145 (80)	142 (23)
Daughter cells	155 (52)	151 (63)	164 (53)	143 (82)	152 (27)

*Authors in [87] used the time between successive budding events to represent the cycle time.

doi:10.1371/journal.pone.0153738.t007

exit from mitosis and divide. Cells with higher activities of Sic1 and/or Cdh1 or lower levels of Clb2 may be able to divide, but cells at the other extreme will be arrested in anaphase.

In S9 Fig we show that *CLB2-dbΔ GAL-SIC1 (CLB5 in place)* mutant cells growing in raffinose (Sic1 not produced) have comparable viability to *CLB2-dbΔ clb5Δ GAL-SIC1* cells growing in raffinose, because Clb5 protein is mostly degraded by APC/Cdc20 by the time the *CLB2-dbΔ CLB5* cells are exiting (or not) from mitosis. Although *CLB2-dbΔ CLB5 GAL-SIC1* cells are inviable in glucose medium (rapidly growing cells that are not producing Sic1), there is anecdotal evidence that these cells are partially viable when cultured on poor growth medium, like raffinose [86]. So, our stochastic model is consistent with a conclusion that *CLB2-dbΔ CLB5* cells are on the cusp of viability/inviability when growing on poor carbon sources.

Discussion

We have presented a “standard component modeling” strategy for protein regulatory networks by grouping proteins into three classes according to the presumptive time scales of the reactions involved. We assume that class-1 proteins change slowly in time due to synthesis and degradation, and we describe these changes by pseudo-linear ODEs. With good estimates for the rate constants of synthesis and degradation, the dynamics of class-1 variables can be compared directly to experimental data (i.e., time-series data). Class-2 proteins change more rapidly in time due to protein modifications and are described by nonlinear ODEs employing the soft-Heaviside function, $H(x) = 1/(1+e^{-x})$. The soft-Heaviside function gives us many of the advantages of hybrid Boolean-ODE models (e.g., the piecewise linear ODE models of Leon Glass and coworkers [8]) while retaining the powerful analytical tools available for nonlinear ODEs (e.g., bifurcation theory). Class-3 variables describe strongly bound protein complexes that form rapidly from two subunits; hence, the total amounts of the bound and free forms can be easily computed using the “max” function.

The SCM approach has many advantages. Its basic assumptions are natural because these three classes of protein species are commonly encountered in PRNs. The modularity of the components allows modelers to build mathematical representations of complicated networks in a controlled and logical fashion. Modularity also renders the models easily modifiable and extensible. Because the models are rendered in terms of nonlinear ODEs, the modeler has access to well-tested software for simulation, analysis (bifurcation theory, sensitivity analysis), and parameter estimation. Furthermore, the SCM formalism is readily adapted to stochastic simulation by chemical Langevin equations (CLEs), and we have shown how to incorporate transcription-translation coupling into the CLEs to account for fluctuations at the mRNA level without necessarily having explicit mRNA species in the model.

The vulnerabilities of the approach should also be clearly recognized. Although the soft-Heaviside function conveniently represents a sigmoidal signal-response curve, it has no basis in biochemical reaction mechanisms, and the interaction coefficients (ω_{ji} 's) are not related to any measurable reaction rate constants. The use of the “max” function to describe class-3 variables

is even more restrictive. Strictly speaking it applies only to strongly bound dimeric complexes that form rapidly and reversibly. It can be extended to other special cases, but it is easy to imagine realistic situations in which the max-function approximation gives unsatisfactory results.

Nonetheless, the modularity of an SCM allows problematic situations to be spotted and readily repaired. For example, if protein components in a mechanism form competing binary and ternary (and higher) complexes, the max functions proposed here can be replaced by a set of nonlinear algebraic equations (the equilibrium binding equations) for the amounts of the complexes. In this case, the SCM becomes a system of differential-algebraic equations (DAEs), and there are well-tested numerical algorithms (e.g., DASSL [97]) for solving DAEs accurately and efficiently. Alternately, one could replace the equilibrium binding equations by ODEs for the complexes themselves, and solve the larger system of nonlinear ODEs by a suitable “stiff” ODE solver. It may also be advisable in some circumstances to replace the soft-Heaviside function, governing class-2 variables, by a more realistic (biochemically based) nonlinearity, e.g., a Hill function for transcription factor-binding to gene promoters. The modularity of SCMs makes such replacements easy.

Indeed, we do not want to give the impression that SCM is a take-it-or-leave-it approach. It would be quite reasonable for parts of a model to be SCM-like and other parts more biochemically realistic. A model may start life as a Boolean network capturing the gross qualitative features of a physiological trait, be translated into an SCM to provide more quantitative details for comparison to experiments, and later get fleshed out with full biochemical verisimilitude. Alternatively, we may wish to extend a biochemically detailed model, like Chen-2004 for the budding yeast cell cycle, to new aspects of the control system. Mechanistic proposals for these new aspects can be grafted on to the full model using the SCM approach for a quick appraisal. If biochemical details are lacking, the new parts of the model will coexist quite peacefully with the original ODE model. If the biochemistry is known and relevant, the SCM modules can be swapped out for something more realistic.

We have applied this approach to a detailed molecular mechanism of cell cycle control in budding yeast. Compared to a model based on traditional biochemical kinetics [41], our new model based on “standard components” has fewer parameters that need to be estimated from experimental data. Furthermore, in our experience, the standard component model (SCM) is easier to build, easier to modify and extend, and easier to parameterize by fitting the model to experimental data. Nonetheless, the SCM is just as accurate as the detailed biochemical model [41], reproducing the phenotypes of 94% of the mutant budding yeast strains in our test collection. A major advantage of the SCM is that it can easily be converted to a stochastic model that can account for cell-to-cell variability in wild-type and mutant strains of budding yeast. The stochastic SCM accounts for the impact of mRNA fluctuations on protein fluctuations, without requiring explicit modeling of mRNA dynamics. Because the stochastic SCM is formulated in terms of stochastic differential equations of the Langevin type, it can be simulated very efficiently compared to Gillespie’s “stochastic simulation algorithm” [14] applied to a fully detailed biochemical kinetic model.

Although the SCM approach has proved successful in describing cell cycle regulation by cyclin-dependent kinases, its potential for describing other PRNs must await future attempts to apply the approach to other problems (e.g., for circadian rhythms, epidermal growth factor signaling, epithelial-to-mesenchymal cell transition).

Methods

See [S9 Text](#) for our simulation methods. All simulations (both deterministic and stochastic) were done by Euler’s explicit, first-order method with step size $\Delta t = 0.01$ min. In [S10 Text](#) we provide evidence that this step size is small enough to obtain reliable results.

Supporting Information

S1 Fig. The soft-Heaviside function. $H(\sigma W) = 1/(1 + e^{-\sigma W})$ varies smoothly from 0 to 1 as a function of increasing W . The parameter σ determines the steepness of the function. The soft-Heaviside function approaches the true Heaviside function as $\sigma \rightarrow \infty$.
(EPS)

S2 Fig. Two-parameter bifurcation diagrams for the Start models. Upper panel: The two-parameter bifurcation diagrams show similar regions of bistability between the two models when the synthesis rate of Cln3 ($k_{s,n3}$) and (fixed) cell volume are varied. Lower panel: However, at large synthesis rates of ClbS ($k_{s,bs}$), the values of (fixed) cell volume that exhibit bistability are different between the two models. The value of $k_{s,bs}$ used in both models is $0.3 \text{ fl}^{-1} \text{ min}^{-1}$ (taken from the value used by Barik *et al.* [27]). At this value, both models show a similar bistability region when (fixed) cell volume is varied.
(PDF)

S3 Fig. T_2 durations of cells with different initial cell size (V_0) from the Start models. In both models, the gap between START and the G₁/S transition, $T_2 = T_{G1} - T_1$, is nearly independent of birth size.
(EPS)

S4 Fig. Steady-state distributions of Cln3, SBF and ClbS in Start models at fixed cell size. Black lines: MultiP model in [S1 Text](#); red lines: stochastic SCM model in [S3 Text](#); blue lines: stochastic SCM without mRNA noise (i.e., all $\zeta_2(t) = 0$ in [S3 Text](#)); green lines: stochastic SCM with explicit mRNA species, as described in [S4 Text](#). The steady-state distributions at fixed V are shown as the Kernel density estimation. $V = 10 \text{ fl}$ is a very small yeast cell, $V = 35 \text{ fl}$ corresponds to cells that have executed the START transition. At large V , the distributions from the SCM without mRNA noise are much narrower than the distributions from the other models. Means of SBF molecules from the three SCM models deviate from the SBF mean from the MultiP model (panel C).
(EPS)

S5 Fig. Stochastic simulations of the relation between initial cell size (V_0) and average cell age at the Start transition (T_1) (upper panel) and average cell age at the G₁/S transition (T_{G1}) (lower panel) for the Start models. The average values of T_1 and T_{G1} agree well between the models and show similar patterns to the deterministic simulations in [Fig 4](#) of the main text.
(EPS)

S6 Fig. Distributions of cell age at the Start transition (T_1) and at the G₁/S transition (T_{G1}) from the Start models. Distributions of T_1 and T_{G1} with initial cell size (V_0) of 10, 35, and 50 fl from [Figs 6](#) and [7](#) of the main text are shown as the Kernel density estimation. Similar to what we found in [Figs 6](#) and [7](#), the distributions from the SCM (red) and the MultiP model (black) agree well at small V_0 (e.g., $V_0 = 10 \text{ fl}$). The SCM without mRNA noise (blue) always exhibits narrower deviation than the other models. The SCM with explicit mRNA species (green) shows better agreement to the MultiP model than the SCM and the SCM without mRNA noise at large V_0 (e.g., $V_0 = 35$ and 50 fl).
(EPS)

S7 Fig. Distributions of cell cycle properties from the full cell cycle SCM. Distributions of some cell cycle properties from [Fig 10](#) of the main text: cell cycle time (T_c), time from cell birth to START (T_1), and volume at cell birth (V_{birth}), are shown as the Kernel density estimation. T_1 duration predicted from the full stochastic simulation (Panel D, black) is markedly shorter

than the results from the model without mRNA fluctuations (Panel D, red) and the extrinsic-only model (Panel D, blue) (see main text for discussion).

(EPS)

S8 Fig. Average values of G_1 phase (T_{G1}) and Start phase (T_1) durations of daughter cells calculated from data collected from simulations of individual cells binned in 2 fL volume intervals from our stochastic simulations of the full cell cycle model. Red dots: T_{G1} from [Fig 11](#) (main text); blue dots: T_1 , the time from cell birth to SBF reaching 50% of its maximal activity. The gap between the two lines confirms the experimental observation that $T_2 = T_{G1} - T_1$ is relatively constant.

(EPS)

S9 Fig. Cycle time distributions for *CLB2-dbΔ GAL-SIC1* cells (*CLB5* in place) in raffinose medium. Cumulative distributions of cycle times for *CLB2-dbΔ GAL-SIC1* cells (dashed line) and *CLB2-dbΔ clb5Δ GAL-SIC1* cells (solid line; from [Fig 12](#) of the main text) growing in raffinose medium (*GAL-SIC1* is “off”). The ordinate, $P(t)$, is the probability that a simulated cell has a cycle time greater than t . Our stochastic model is consistent with Cross’s suggestion that the inviability of *CLB2-dbΔ GAL-SIC1* cells growing on glucose medium is partially rescued by growth on alternative poor-carbon sources (e.g., raffinose rather than glucose) [[86](#)].

(EPS)

S1 File. C++ and XPP codes.

(ZIP)

S1 Table. Parameter values for the multisite phosphorylation model of the Start transition.

(DOCX)

S2 Table. Initial conditions for simulations of the multisite phosphorylation model of the Start transition in [Figs 3](#) and [5](#).

(DOCX)

S3 Table. List of mutant strains used to test our deterministic model of the full cell cycle system.

(DOCX)

S4 Table. Parameter changes and initial conditions used to simulate mutant alleles.

(DOCX)

S5 Table. Rules for inviable mutant phenotypes.

(DOCX)

S6 Table. Inconsistencies between simulations and observations.

(DOCX)

S1 Text. Equations for the multisite phosphorylation model of the Start transition.

(DOC)

S2 Text. Derivation of the mRNA-inherited noise term.

(DOC)

S3 Text. Equations for the stochastic SCM of the Start transition.

(DOC)

S4 Text. Equations for the stochastic SCM of the Start transition with explicit mRNA species.

(DOC)

S5 Text. Mutant simulations and discussion of problems.

(DOC)

S6 Text. Model conversion.

(DOC)

S7 Text. The mRNA-inherited noise term of the full budding yeast cell cycle model.

(DOC)

S8 Text. The effects of the parameters $\langle m_{\min} \rangle$ on the model.

(DOC)

S9 Text. Simulation methods.

(DOC)

S10 Text. The effects of the integration step size (Δt) on the model.

(DOC)

Acknowledgments

This work was supported in part by a fellowship to TL from the Higher Educational Strategic Scholarships for Frontier Research Network (SFR) of the Thai government, and by grants from the US National Institutes of Health: 5R01GM078989-06 (to JJT and WTB) and 5R01GM095955-01 (to T.M. Murali and JJT). We are grateful to two anonymous reviewers for their advice in improving this paper.

Author Contributions

Conceived and designed the experiments: TL KC WTB JJT. Performed the experiments: TL KC. Analyzed the data: TL KC WTB JJT. Contributed reagents/materials/analysis tools: TL KC. Wrote the paper: TL KC WTB JJT.

References

1. Brazhnik P, de la Fuente A, Mendes P. Gene networks: how to put the function in genomics. *Trends Biotechnol.* 2002; 20(11):467–72. PMID: [12413821](#)
2. Albert R, Othmer HG. The topology of the regulatory interactions predicts the expression pattern of the segment polarity genes in *Drosophila melanogaster*. *J Theor Biol.* 2003; 223(1):1–18. PMID: [12782112](#)
3. Fauré A, Naldi A, Lopez F, Chaouiya C, Ciliberto A, Thieffry D. Modular logical modelling of the budding yeast cell cycle. *Mol Biosyst.* 2009; 5(12):1787–96. doi: [10.1039/B910101m](#) PMID: [19763337](#)
4. Li F, Long T, Lu Y, Ouyang Q, Tang C. The yeast cell-cycle network is robustly designed. *Proc Natl Acad Sci U S A.* 2004; 101(14):4781–6. PMID: [15037758](#)
5. Bray D, Bourret RB, Simon MI. Computer simulation of the phosphorylation cascade controlling bacterial chemotaxis. *Mol Biol Cell.* 1993; 4(5):469–82. PMID: [8334303](#)
6. Novak B, Tyson JJ. Numerical analysis of a comprehensive model of M-phase control in *Xenopus* oocyte extracts and intact embryos. *J Cell Sci.* 1993; 106(4):1153–68.
7. Karr JR, Williams AH, Zucker JD, Raue A, Steiert B, Timmer J, et al. Summary of the DREAM8 parameter estimation challenge: toward parameter identification for whole-cell models. *PLoS Comput Biol.* 2015; 11(5):e1004096. doi: [10.1371/journal.pcbi.1004096](#) PMID: [26020786](#)
8. Glass L, Kauffman SA. The logical analysis of continuous, non-linear biochemical control networks. *J Theor Biol.* 1973; 39(1):103–29. PMID: [4741704](#)
9. Alon U. *An introduction to systems biology: design principles of biological circuits.* Boca Raton, FL: Chapman & Hall/CRC; 2007. 301 p.
10. Mason J, Linsay PS, Collins JJ, Glass L. Evolving complex dynamics in electronic models of genetic networks. *Chaos.* 2004; 14(3):707–15. PMID: [15446982](#)

11. Casey R, de Jong H, Gouze JL. Piecewise-linear models of genetic regulatory networks: equilibria and their stability. *J Math Biol.* 2006; 52(1):27–56. PMID: [16195929](#)
12. Singhania R, Sramkoski RM, Jacobberger JW, Tyson JJ. A hybrid model of mammalian cell cycle regulation. *PLoS Comput Biol.* 2011; 7(2):e1001077. doi: [10.1371/journal.pcbi.1001077](#) PMID: [21347318](#)
13. Gillespie DT. A general method for numerically simulating the stochastic time evolution of coupled chemical reactions. *J Comput Phys.* 1976; 22(4):403–34.
14. Gillespie DT. Stochastic simulation of chemical kinetics. *Annu Rev Phys Chem.* 2007; 58:35–55. PMID: [17037977](#)
15. Mura I, Csikász-Nagy A. Stochastic Petri Net extension of a yeast cell cycle model. *J Theor Biol.* 2008; 254(4):850–60. doi: [10.1016/j.jtbi.2008.07.019](#) PMID: [18703074](#)
16. Braunewell S, Bornholdt S. Superstability of the yeast cell-cycle dynamics: ensuring causality in the presence of biochemical stochasticity. *J Theor Biol.* 2007; 245(4):638–43. PMID: [17204290](#)
17. Zhang Y, Qian M, Ouyang Q, Deng M, Li F, Tang C. Stochastic model of yeast cell-cycle network. *Physica D.* 2006; 219(1):35–9.
18. Ciliberto A, Capuani F, Tyson JJ. Modeling networks of coupled enzymatic reactions using the total quasi-steady state approximation. *PLoS Comput Biol.* 2007; 3(3):e45. PMID: [17367203](#)
19. Sabouri-Ghomi M, Ciliberto A, Kar S, Novak B, Tyson JJ. Antagonism and bistability in protein interaction networks. *J Theor Biol.* 2008; 250(1):209–18. PMID: [17950756](#)
20. Tyson JJ, Novak B. Functional motifs in biochemical reaction networks. *Annu Rev Phys Chem.* 2010; 61:219–40. doi: [10.1146/annurev.physchem.012809.103457](#) PMID: [20055671](#)
21. Hong T, Xing J, Li L, Tyson JJ. A mathematical model for the reciprocal differentiation of T helper 17 cells and induced regulatory T cells. *PLoS Comput Biol.* 2011; 7(7):e1002122. doi: [10.1371/journal.pcbi.1002122](#) PMID: [21829337](#)
22. Mjolsness E, Sharp DH, Reinitz J. A connectionist model of development. *J Theor Biol.* 1991; 152(4):429–53. PMID: [1758194](#)
23. Molinelli EJ, Korkut A, Wang W, Miller ML, Gauthier NP, Jing X, et al. Perturbation biology: inferring signaling networks in cellular systems. *PLoS Comput Biol.* 2013; 9(12):e1003290. doi: [10.1371/journal.pcbi.1003290](#) PMID: [24367245](#)
24. Ferrell JE Jr. Tripping the switch fantastic: how a protein kinase cascade can convert graded inputs into switch-like outputs. *Trends Biochem Sci.* 1996; 21(12):460–6. PMID: [9009826](#)
25. Goldbeter A, Koshland DE Jr. An amplified sensitivity arising from covalent modification in biological systems. *Proc Natl Acad Sci U S A.* 1981; 78(11):6840–4. PMID: [6947258](#)
26. Kapuy O, Barik D, Sananes MR, Tyson JJ, Novak B. Bistability by multiple phosphorylation of regulatory proteins. *Prog Biophys Mol Biol.* 2009; 100(1–3):47–56. doi: [10.1016/j.pbiomolbio.2009.06.004](#) PMID: [19523976](#)
27. Barik D, Baumann WT, Paul MR, Novak B, Tyson JJ. A model of yeast cell-cycle regulation based on multisite phosphorylation. *Mol Syst Biol.* 2010; 6:405. doi: [10.1038/msb.2010.55](#) PMID: [20739927](#)
28. Yang L, MacLellan WR, Han Z, Weiss JN, Qu Z. Multisite phosphorylation and network dynamics of cyclin-dependent kinase signaling in the eukaryotic cell cycle. *Biophys J.* 2004; 86(6):3432–43. PMID: [15189845](#)
29. Costanzo M, Nishikawa JL, Tang X, Millman JS, Schub O, Breikreuz K, et al. CDK activity antagonizes Whi5, an inhibitor of G₁/S transcription in yeast. *Cell.* 2004; 117(7):899–913. PMID: [15210111](#)
30. de Bruin RA, McDonald WH, Kalashnikova TI, Yates J 3rd, Wittenberg C. Cln3 activates G₁-specific transcription via phosphorylation of the SBF bound repressor Whi5. *Cell.* 2004; 117(7):887–98. PMID: [15210110](#)
31. Cross FR, Archambault V, Miller M, Klovstad M. Testing a mathematical model of the yeast cell cycle. *Mol Biol Cell.* 2002; 13(1):52–70. PMID: [11809822](#)
32. Hartwell LH, Unger MW. Unequal division in *Saccharomyces cerevisiae* and its implications for the control of cell division. *J Cell Biol.* 1977; 75(2 Pt 1):422–35. PMID: [400873](#)
33. Johnston GC, Pringle JR, Hartwell LH. Coordination of growth with cell division in the yeast *Saccharomyces cerevisiae*. *Exp Cell Res.* 1977; 105(1):79–98. PMID: [320023](#)
34. Polymenis M, Schmidt EV. Coupling of cell division to cell growth by translational control of the G₁ cyclin CLN3 in yeast. *Genes Dev.* 1997; 11(19):2522–31. PMID: [9334317](#)
35. Schmoller KM, Turner JJ, Kőivomägi M, Skotheim JM. Dilution of the cell cycle inhibitor Whi5 controls budding-yeast cell size. *Nature.* 2015; 526(7572):268–72. doi: [10.1038/nature14908](#) PMID: [26390151](#)
36. Charvin G, Oikonomou C, Siggia ED, Cross FR. Origin of irreversibility of cell cycle start in budding yeast. *PLoS Biol.* 2010; 8(1):e1000284. doi: [10.1371/journal.pbio.1000284](#) PMID: [20087409](#)

37. Wagner MV, Smolka MB, de Bruin RA, Zhou H, Wittenberg C, Dowdy SF. Whi5 regulation by site specific CDK-phosphorylation in *Saccharomyces cerevisiae*. PLoS ONE. 2009; 4(1):e4300. doi: [10.1371/journal.pone.0004300](https://doi.org/10.1371/journal.pone.0004300) PMID: [19172996](https://pubmed.ncbi.nlm.nih.gov/19172996/)
38. Di Talia S, Skotheim JM, Bean JM, Siggia ED, Cross FR. The effects of molecular noise and size control on variability in the budding yeast cell cycle. Nature. 2007; 448(7156):947–51. PMID: [17713537](https://pubmed.ncbi.nlm.nih.gov/17713537/)
39. Pedraza JM, Paulsson J. Effects of molecular memory and bursting on fluctuations in gene expression. Science. 2008; 319(5861):339–43. doi: [10.1126/science.1144331](https://doi.org/10.1126/science.1144331) PMID: [18202292](https://pubmed.ncbi.nlm.nih.gov/18202292/)
40. Gillespie DT. The chemical Langevin equation. J Chem Phys. 2000; 113(1):297–306.
41. Chen KC, Calzone L, Csikasz-Nagy A, Cross FR, Novak B, Tyson JJ. Integrative analysis of cell cycle control in budding yeast. Mol Biol Cell. 2004; 15(8):3841–62. PMID: [15169868](https://pubmed.ncbi.nlm.nih.gov/15169868/)
42. Toth A, Queralt E, Uhlmann F, Novak B. Mitotic exit in two dimensions. J Theor Biol. 2007; 248(3):560–73. PMID: [17659305](https://pubmed.ncbi.nlm.nih.gov/17659305/)
43. Chen KC, Csikasz-Nagy A, Gyorffy B, Val J, Novak B, Tyson JJ. Kinetic analysis of a molecular model of the budding yeast cell cycle. Mol Biol Cell. 2000; 11(1):369–91. PMID: [10637314](https://pubmed.ncbi.nlm.nih.gov/10637314/)
44. Novak B, Csikasz-Nagy A, Gyorffy B, Chen KC, Tyson JJ. Mathematical model of the fission yeast cell cycle with checkpoint controls at the G₁/S, G₂/M and metaphase/anaphase transitions. Biophys Chem. 1998; 72(1–2):185–200. PMID: [9652094](https://pubmed.ncbi.nlm.nih.gov/9652094/)
45. Tyson JJ, Novak B. Irreversible transitions, bistability and checkpoint controls in the eukaryotic cell cycle: a systems-level understanding. Handbook of Systems Biology. 2012:265–85.
46. Mendenhall MD, Hodge AE. Regulation of Cdc28 cyclin-dependent protein kinase activity during the cell cycle of the yeast *Saccharomyces cerevisiae*. Microbiol Mol Biol Rev. 1998; 62(4):1191–243. PMID: [9841670](https://pubmed.ncbi.nlm.nih.gov/9841670/)
47. Schwob E, Bohm T, Mendenhall MD, Nasmyth K. The B-type cyclin kinase inhibitor p40^{SIC1} controls the G₁ to S transition in *S. cerevisiae*. Cell. 1994; 79(2):233–44. PMID: [7954792](https://pubmed.ncbi.nlm.nih.gov/7954792/)
48. Deshaies RJ, Chau V, Kirschner M. Ubiquitination of the G₁ cyclin Cln2p by a Cdc34p-dependent pathway. EMBO J. 1995; 14(2):303–12. PMID: [7835341](https://pubmed.ncbi.nlm.nih.gov/7835341/)
49. Wijnen H, Futcher B. Genetic analysis of the shared role of CLN3 and BCK2 at the G₁-S transition in *Saccharomyces cerevisiae*. Genetics. 1999; 153(3):1131–43. PMID: [10545447](https://pubmed.ncbi.nlm.nih.gov/10545447/)
50. Ferrezuelo F, Aldea M, Futcher B. Bck2 is a phase-independent activator of cell cycle-regulated genes in yeast. Cell Cycle. 2009; 8(2):239–52. PMID: [19158491](https://pubmed.ncbi.nlm.nih.gov/19158491/)
51. Taberner FJ, Quilis I, Igual JC. Spatial regulation of the start repressor Whi5. Cell Cycle. 2009; 8(18):3010–8. PMID: [19713766](https://pubmed.ncbi.nlm.nih.gov/19713766/)
52. Epstein CB, Cross FR. Genes that can bypass the CLN requirement for *Saccharomyces cerevisiae* cell cycle START. Mol Cell Biol. 1994; 14(3):2041–7. PMID: [8114735](https://pubmed.ncbi.nlm.nih.gov/8114735/)
53. Amon A, Tyers M, Futcher B, Nasmyth K. Mechanisms that help the yeast cell cycle clock tick: G₂ cyclins transcriptionally activate G₂ cyclins and repress G₁ cyclins. Cell. 1993; 74(6):993–1007. PMID: [8402888](https://pubmed.ncbi.nlm.nih.gov/8402888/)
54. Koch C, Schleiffer A, Ammerer G, Nasmyth K. Switching transcription on and off during the yeast cell cycle: Cln/Cdc28 kinases activate bound transcription factor SBF (Swi4/Swi6) at start, whereas Clb/Cdc28 kinases displace it from the promoter in G₂. Genes Dev. 1996; 10(2):129–41. PMID: [8566747](https://pubmed.ncbi.nlm.nih.gov/8566747/)
55. Skotheim JM, Di Talia S, Siggia ED, Cross FR. Positive feedback of G₁ cyclins ensures coherent cell cycle entry. Nature. 2008; 454(7202):291–6. doi: [10.1038/nature07118](https://doi.org/10.1038/nature07118) PMID: [18633409](https://pubmed.ncbi.nlm.nih.gov/18633409/)
56. Cvrckova F, Nasmyth K. Yeast G₁ cyclins CLN1 and CLN2 and a GAP-like protein have a role in bud formation. EMBO J. 1993; 12(13):5277–86. PMID: [8262070](https://pubmed.ncbi.nlm.nih.gov/8262070/)
57. Archambault V, Li CX, Tackett AJ, Wasch R, Chait BT, Rout MP, et al. Genetic and biochemical evaluation of the importance of Cdc6 in regulating mitotic exit. Mol Biol Cell. 2003; 14(11):4592–604. PMID: [12960422](https://pubmed.ncbi.nlm.nih.gov/12960422/)
58. Calzada A, Sacristan M, Sanchez E, Bueno A. Cdc6 cooperates with Sic1 and Hct1 to inactivate mitotic cyclin-dependent kinases. Nature. 2001; 412(6844):355–8. PMID: [11460169](https://pubmed.ncbi.nlm.nih.gov/11460169/)
59. Verma R, Feldman RM, Deshaies RJ. SIC1 is ubiquitinated in vitro by a pathway that requires CDC4, CDC34, and cyclin/CDK activities. Mol Biol Cell. 1997; 8(8):1427–37. PMID: [9285816](https://pubmed.ncbi.nlm.nih.gov/9285816/)
60. Stuart D, Wittenberg C. CLB5 and CLB6 are required for premeiotic DNA replication and activation of the meiotic S/M checkpoint. Genes Dev. 1998; 12(17):2698–710. PMID: [9732268](https://pubmed.ncbi.nlm.nih.gov/9732268/)
61. Amon A. Regulation of B-type cyclin proteolysis by Cdc28-associated kinases in budding yeast. EMBO J. 1997; 16(10):2693–702. PMID: [9184216](https://pubmed.ncbi.nlm.nih.gov/9184216/)

62. Jaspersen SL, Charles JF, Morgan DO. Inhibitory phosphorylation of the APC regulator Hct1 is controlled by the kinase Cdc28 and the phosphatase Cdc14. *Curr Biol*. 1999; 9(5):227–36. PMID: [10074450](#)
63. Maher M, Cong F, Kindelberger D, Nasmyth K, Dalton S. Cell cycle-regulated transcription of the CLB2 gene is dependent on Mcm1 and a ternary complex factor. *Mol Cell Biol*. 1995; 15(6):3129–37. PMID: [7760809](#)
64. Knapp D, Bhoite L, Stillman DJ, Nasmyth K. The transcription factor Swi5 regulates expression of the cyclin kinase inhibitor p40^{SIC1}. *Mol Cell Biol*. 1996; 16(10):5701–7. PMID: [8816483](#)
65. Rudner AD, Murray AW. Phosphorylation by Cdc28 activates the Cdc20-dependent activity of the anaphase-promoting complex. *J Cell Biol*. 2000; 149(7):1377–90. PMID: [10871279](#)
66. Cohen-Fix O, Peters JM, Kirschner MW, Koshland D. Anaphase initiation in *Saccharomyces cerevisiae* is controlled by the APC-dependent degradation of the anaphase inhibitor Pds1p. *Genes Dev*. 1996; 10(24):3081–93. PMID: [8985178](#)
67. Ciosk R, Zachariae W, Michaelis C, Shevchenko A, Mann M, Nasmyth K. An ESP1/PDS1 complex regulates loss of sister chromatid cohesion at the metaphase to anaphase transition in yeast. *Cell*. 1998; 93(6):1067–76. PMID: [9635435](#)
68. Baumer M, Braus GH, Irmiger S. Two different modes of cyclin Clb2 proteolysis during mitosis in *Saccharomyces cerevisiae*. *FEBS Lett*. 2000; 468(2–3):142–8. PMID: [10692575](#)
69. Hwang LH, Lau LF, Smith DL, Mistrot CA, Hardwick KG, Hwang ES, et al. Budding yeast Cdc20: a target of the spindle checkpoint. *Science*. 1998; 279(5353):1041–4. PMID: [9461437](#)
70. Queralt E, Uhlmann F. Cdk-counteracting phosphatases unlock mitotic exit. *Curr Opin Cell Biol*. 2008; 20(6):661–8. doi: [10.1016/j.ceb.2008.09.003](#) PMID: [18845253](#)
71. Queralt E, Lehane C, Novak B, Uhlmann F. Downregulation of PP2A^{Cdc55} phosphatase by separase initiates mitotic exit in budding yeast. *Cell*. 2006; 125(4):719–32. PMID: [16713564](#)
72. Sullivan M, Uhlmann F. A non-proteolytic function of separase links the onset of anaphase to mitotic exit. *Nat Cell Biol*. 2003; 5(3):249–54. PMID: [12598903](#)
73. Stegmeier F, Visintin R, Amon A. Separase, polo kinase, the kinetochore protein Slk19, and Spo12 function in a network that controls Cdc14 localization during early anaphase. *Cell*. 2002; 108(2):207–20. PMID: [11832211](#)
74. Shou W, Seol JH, Shevchenko A, Baskerville C, Moazed D, Chen ZW, et al. Exit from mitosis is triggered by Tem1-dependent release of the protein phosphatase Cdc14 from nucleolar RENT complex. *Cell*. 1999; 97(2):233–44. PMID: [10219244](#)
75. Visintin R, Hwang ES, Amon A. Cfi1 prevents premature exit from mitosis by anchoring Cdc14 phosphatase in the nucleolus. *Nature*. 1999; 398(6730):818–23. PMID: [10235265](#)
76. Shou W, Sakamoto KM, Keener J, Morimoto KW, Traverso EE, Azzam R, et al. Net1 stimulates RNA polymerase I transcription and regulates nucleolar structure independently of controlling mitotic exit. *Mol Cell*. 2001; 8(1):45–55. PMID: [11511359](#)
77. Jaspersen SL, Morgan DO. Cdc14 activates Cdc15 to promote mitotic exit in budding yeast. *Curr Biol*. 2000; 10(10):615–8. PMID: [10837230](#)
78. Mortensen EM, Haas W, Gygi M, Gygi SP, Kellogg DR. Cdc28-dependent regulation of the Cdc5/Polo kinase. *Curr Biol*. 2005; 15(22):2033–7. PMID: [16303563](#)
79. Hu F, Wang Y, Liu D, Li Y, Qin J, Elledge SJ. Regulation of the Bub2/Bfa1 GAP complex by Cdc5 and cell cycle checkpoints. *Cell*. 2001; 107(5):655–65. PMID: [11733064](#)
80. Yeong FM, Lim HH, Padmashree CG, Surana U. Exit from mitosis in budding yeast: biphasic inactivation of the Cdc28-Clb2 mitotic kinase and the role of Cdc20. *Mol Cell*. 2000; 5(3):501–11. PMID: [10882135](#)
81. Wasch R, Cross FR. APC-dependent proteolysis of the mitotic cyclin Clb2 is essential for mitotic exit. *Nature*. 2002; 418(6897):556–62. PMID: [12152084](#)
82. Visintin C, Tomson BN, Rahal R, Paulson J, Cohen M, Taunton J, et al. APC/C-Cdh1-mediated degradation of the Polo kinase Cdc5 promotes the return of Cdc14 into the nucleolus. *Genes Dev*. 2008; 22(1):79–90. doi: [10.1101/gad.1601308](#) PMID: [18172166](#)
83. Visintin R, Craig K, Hwang ES, Prinz S, Tyers M, Amon A. The phosphatase Cdc14 triggers mitotic exit by reversal of Cdk-dependent phosphorylation. *Mol Cell*. 1998; 2(6):709–18. PMID: [9885559](#)
84. Lord PG, Wheals AE. Asymmetrical division of *Saccharomyces cerevisiae*. *J Bacteriol*. 1980; 142(3):808–18. PMID: [6991494](#)
85. Oguz C, Laomettachit T, Chen KC, Watson LT, Baumann WT, Tyson JJ. Optimization and model reduction in the high dimensional parameter space of a budding yeast cell cycle model. *BMC Syst Biol*. 2013; 7(1):53.

86. Cross FR. Two redundant oscillatory mechanisms in the yeast cell cycle. *Dev Cell*. 2003; 4(5):741–52. PMID: [12737808](#)
87. Ball DA, Ahn TH, Wang PY, Chen KC, Cao Y, Tyson JJ, et al. Stochastic exit from mitosis in budding yeast: model predictions and experimental observations. *Cell Cycle*. 2011; 10(6):999–1009. PMID: [21350333](#)
88. Bean JM, Siggia ED, Cross FR. Coherence and timing of cell cycle start examined at single-cell resolution. *Mol Cell*. 2006; 21(1):3–14. PMID: [16387649](#)
89. Ball DA, Marchand J, Poulet M, Baumann WT, Chen KC, Tyson JJ, et al. Oscillatory dynamics of cell cycle proteins in single yeast cells analyzed by imaging cytometry. *PLoS ONE*. 2011; 6(10):e26272. doi: [10.1371/journal.pone.0026272](#) PMID: [22046265](#)
90. Zenklusen D, Larson DR, Singer RH. Single-RNA counting reveals alternative modes of gene expression in yeast. *Nat Struct Mol Biol*. 2008; 15(12):1263–71. doi: [10.1038/nsmb.1514](#) PMID: [19011635](#)
91. Ball DA, Adames NR, Reischmann N, Barik D, Franck CT, Tyson JJ, et al. Measurement and modeling of transcriptional noise in the cell cycle regulatory network. *Cell Cycle*. 2013; 12(19):3203–18. doi: [10.4161/cc.26257](#) PMID: [24013422](#)
92. Kar S, Baumann WT, Paul MR, Tyson JJ. Exploring the roles of noise in the eukaryotic cell cycle. *Proc Natl Acad Sci U S A*. 2009; 106(16):6471–6. doi: [10.1073/pnas.0810034106](#) PMID: [19246388](#)
93. Wang P, Randhawa R, Shaffer CA, Cao Y, Baumann WT. Converting macromolecular regulatory models from deterministic to stochastic formulation. *Proceedings of the 2008 Spring simulation multicongress*; Ottawa, Canada: Society for Computer Simulation International; 2008. p. 385–92.
94. Zheng X-D, Yang X-Q, Tao Y. Bistability, probability transition rate and first-passage time in an autoactivating positive-feedback loop. *PLoS ONE*. 2011; 6(3):e17104. doi: [10.1371/journal.pone.0017104](#) PMID: [21445288](#)
95. Amos BD, Easterling DR, Watson LT, Thacker WI, Castle BS, Trosset MW. Algorithm XXX: QNSTOP—quasi-Newton algorithm for stochastic optimization. *ACM Trans Math Software*. 2016: In press.
96. Ghaemmaghami S, Huh WK, Bower K, Howson RW, Belle A, Dephoure N, et al. Global analysis of protein expression in yeast. *Nature*. 2003; 425(6959):737–41. PMID: [14562106](#)
97. Petzold LR. A description of DASSL: a differential/algebraic system solver. In: Stepleman R, editor. *Scientific computing*. Amsterdam: North-Holland; 1983.